Nonlinear Rossby adjustment in a channel

By K. R. HELFRICH[1], ALLEN C. KUO[2]
AND L. J. PRATT[1]

[1] Department of Physical Oceanography, Woods Hole Oceanographic Institution,
Woods Hole, MA 02543 USA

[2] Department of Applied Physics and Applied Mathematics, Columbia University,
New York, NY 10027 USA

The Rossby adjustment problem for a homogeneous fluid in a channel is solved for large values of the initial depth discontinuity. We begin by analysing the classical dam break problem in which the depth on one side of the discontinuity is zero. An approximate solution for this case can be constructed by assuming semigeostrophic dynamics and using the method of characteristics. This theory is supplemented by numerical solutions to the full shallow water equations. The development of the flow and the final, equilibrium volume transport are governed by the ratio of the Rossby radius of deformation to the channel width, the only non-dimensional parameter. After the dam is destroyed the rotating fluid spills down the dry section of the channel forming a rarefying intrusion which, for northern hemisphere rotation, is banked against the right-hand wall (facing downstream). As the channel width is increased the speed of the leading edge (along the right-hand wall) exceeds the intrusion speed for the non-rotating case, reaching the limiting value of 3.80 times the linear Kelvin wave speed in the upstream basin. On the left side of the channel fluid separates from the sidewall at a point whose speed decreases to zero as the channel width approaches infinity. Numerical computations of the evolving flow show good agreement with the semigeostrophic theory for widths less than about a deformation radius. For larger widths cross-channel accelerations, absent in the semigeostrophic approximation, reduce the agreement. The final equilibrium transport down the channel is determined from the semigeostrophic theory and found to depart from the non-rotating result for channels widths greater than about one deformation radius. Rotation limits the transport to a constant maximum value for channel widths greater than about four deformation radii.

The case in which the initial fluid depth downstream of the dam is non-zero is then examined numerically. The leading rarefying intrusion is now replaced by a Kelvin shock, or bore, whose speed is substantially less than the zero-depth intrusion speed. The shock is either straight across the channel or attached only to the right-hand wall depending on the channel width and the additional parameter, the initial depth difference. The shock speeds and amplitudes on the right-hand wall, for fixed downstream depth, increase above the non-rotating values with increasing channel width. However, rotation reduces the speed of a shock of given amplitude below the non-rotating case. We also find evidence of resonant generation of Poincaré waves by the bore. Shock characteristics are compared to theories of rotating shocks and qualitative agreement is found except for the change in potential vorticity across the shock, which is very sensitive to the model dissipation. Behind the leading shock the flow evolves in much the same way as described by linear theory except for the generation of strongly nonlinear transverse oscillations and rapid advection down the

right-hand channel wall of fluid originally upstream of the dam. Final steady-state transports decrease from the zero upstream depth case as the initial depth difference is decreased.

---

1. Introduction

The existence of rotationally influenced, hydraulically driven flows in deep ocean straits has been known for some time. These flows can be strongly time-dependent, a feature which hinders interpretation in terms of rotating, hydraulic theory (e.g. Whitehead, Leetma & Knox 1974; Gill 1977). Prominent examples include deep overflows of the Denmark Strait (Smith 1976) and the Faroe Bank Channel (Cederlf, Lundberg & Sterhus 1989). The ultimate understanding of such complicated flows will require reference to idealized models in which generic transients can be isolated and studied. In non-rotating hydraulics, Long's towing experiments (Long 1954, 1955, 1970) and the classical dam break problem (Stoker 1957) have provided a foundation for investigating more complex phenomena. In geophysical fluid dynamics, the classical Rossby adjustment problem (see Gill 1982) and its extension to a channel setting (Gill 1976; Hermann, Rhines & Johnson 1989; Tomasson & Melville 1992) have played a similar role. In the latter, a cross-channel barrier separating two semi-infinite regions of homogeneous fluid of different depths is destroyed, causing the deeper fluid to intrude into the shallower fluid. Gill (1976) solved a linearized version of this problem (assuming an infinitesimal depth difference across the barrier) and showed how a steady current was set up by Kelvin waves moving away from the barrier. The Kelvin wave propagating into the shallower fluid is trapped at the right-hand wall while the Kelvin wave moving into the deeper fluid is trapped at the left wall. The resulting steady flow approaches the section of the initial barrier along the left wall, crosses the channel at that section, and continues along the right wall.

Hermann *et al.* (1989, referred to as HRJ) later extended the solution to cases where the depth difference was small but finite. For large times the Kelvin waves of the linear solution have propagated far from the dam site leaving behind a geostrophically adjusted state (the steady solution to the linear problem). Subsequent nonlinear advection of the potential vorticity front down both sides of the channel occurs. HRJ examined the complexities of the slow time scale evolution of this potential vorticity front using contour dynamics and numerical solutions to the full shallow water equations. Tomasson & Melville (1992) also studied the problem in the weakly nonlinear limit, but added the effects of weak non-hydrostatic dispersion. They focused on determining when the evolution cannot be separated into a linear wave regime followed by nonlinear effects on a slow time scale. They also explored the nonlinear evolution of the leading solitary-like Kelvin wave and showed that it could force Poincaré waves by a direct resonance mechanism described by Melville, Tomasson & Renouard (1989).

The assumption of small initial depth change is a feature which limits the hydraulic behaviour, that is strong departures from geostrophy in the along-channel momentum balance leading to shocks, rarefaction waves, and certain types of separation phenomena. The purpose of the work described herein is to explore the strongly nonlinear, time-dependent regimes created when the depth difference across the barrier is not small. We perform calculations over a range of channel widths and depth differences beginning with the case of zero downstream depth: the dam break in a

rotating channel. An assumption of semigeostrophy (meaning a geostrophic balance in cross-channel but not along-channel momentum) allows an approximate solution based on the method of characteristics and conservation of Kelvin wave Riemann invariants. The sole dimensionless parameter for this case is the ratio of the channel width to the Rossby radius of deformation based on the initial upstream depth. Small values produce flows similar to the classical non-rotating dam break experiment, as described in Stoker (1957). Larger values produce an assortment of interesting features, including separation of the current from the left sidewall (facing downstream), formation of a rarefying intrusion along the right sidewall, and departures of the speeds of the separation point and the intrusion nose below and above the corresponding non-rotating values. Results are compared to numerical simulations based on the full, two-dimensional shallow water equations. The dam break problem allows us to explore fundamental issues arising from the presence of flow separation during geostrophic adjustment. In addition, comparison with the numerical solution provides a measure of the validity of semigeostrophic theory.

We also investigate cases in which the downstream depth is non-zero. The resulting adjustment is complicated by the fact that the intrusion contains a bore (a moving hydraulic jump) leading to non-conservation of potential vorticity. The resulting formation of regions of non-uniform potential vorticity render the characteristic approach much less tractable due to the difficulty in formulating shock-joining conditions. Hence, our solutions are based entirely on numerical simulation. The leading bore may extend across the channel and intersect both walls, or it may be attached only to the right-hand wall. In both cases the bore results in a strong off-shore jet. Bore speeds and amplitudes are found to increase with increasing channel width for a fixed downstream depth. Many of these features are consistent with Fedorov & Melville's (1996, referred to as FM) theory for bores propagating along a coastline. However, the theory slightly overpredicts the bore speeds. Lagrangian advection of new fluid down the channel is discussed.

The solution to the dam break problem also allows investigation of the concept of 'geostrophic control' (Toulany & Garrett 1984), essentially a bound on the volume transport between two rotating reservoirs with unequal surface levels. The bound is proportional to the square of the difference in interior surface elevations between the two reservoirs. A connection with the present problem can be made by thinking of the regions upstream and downstream of the original barrier in our rotating channel. As we will show, the asymptotic ($t \to \infty$) flow that develops is steady and uniform in the along-channel direction, provided the channel width is finite. Therefore the final elevation difference between the two 'reservoirs' is zero and the bound fails. However, we will also show that the bound is valid when based on the initial elevation difference. Moreover, in the limit of infinite channel width, the asymptotic flow does not become longitudinally uniform but, instead, preserves the initial elevation difference between reservoirs. Here the transport bound exactly matches the actual transport.

The formulation of the problem and the semigeostrophic approximation are addressed in §2. Method of characteristic solutions to the semigeostophic theory for the case of zero downstream depth are developed in §3. These solutions are then discussed and compared to numerical solutions of the full nonlinear shallow water equations in §4. The numerical study of the non-zero downstream depth problem is presented in §5. In §6 we discuss the results and compare them with several studies (Stern, Whitehead & Hua 1982; Kubokawa & Hanawa 1984*a, b*; Griffiths & Hopfinger 1983) of two-layer Rossby adjustment along a coast.

2. Mathematical formulation and the semigeostrophic limit

Consider a shallow, homogeneous layer of fluid contained in a channel which rotates in the horizontal (x, y)-plane at angular speed $f/2$, $f > 0$. The channel bottom is horizontal and the cross-section rectangular. The motion is governed by the inviscid shallow water equations (in dimensionless form)

$$\delta^2 \left(\frac{\partial u}{\partial t} + u\frac{\partial u}{\partial x} + v\frac{\partial u}{\partial y} \right) - v = -\frac{\partial d}{\partial x}, \tag{2.1}$$

$$\frac{\partial v}{\partial t} + u\frac{\partial v}{\partial x} + v\frac{\partial v}{\partial y} + u = -\frac{\partial d}{\partial y}, \tag{2.2}$$

$$\frac{\partial d}{\partial t} + \frac{\partial}{\partial x}(ud) + \frac{\partial}{\partial y}(vd) = 0. \tag{2.3}$$

The layer thickness d is scaled by the initial depth behind the dam D, x (cross-channel dimension) by the deformation radius $\sqrt{gD}/f$, y (along-channel dimension) by the length scale L and time t by $(L/\sqrt{gD})$. The along-channel velocity v is scaled by $\sqrt{gD}$, the cross-channel velocity u by $\delta\sqrt{gD}$ and $\delta = \sqrt{gD}/fL$.

One consequence of (2.1)–(2.3) is that the potential vorticity q is conserved following fluid parcels,

$$\frac{\partial q}{\partial t} + u\frac{\partial q}{\partial x} + v\frac{\partial q}{\partial y} = 0 \tag{2.4}$$

where

$$q = \frac{1 + \partial v/\partial x - \delta^2 \partial u/\partial y}{d}. \tag{2.5}$$

We first investigate the breaking of a dam in an infinitely long channel of constant width w and zero depth downstream of the dam. The initial and boundary conditions are

$$u(x, y, 0) = 0, \tag{2.6}$$

$$v(x, y, 0) = 0, \tag{2.7}$$

$$d(x, y, 0) = \begin{cases} 1, & y < 0 \\ 0, & y > 0, \end{cases} \tag{2.8}$$

$$u(\pm w/2, y, t) = 0. \tag{2.9}$$

The parameter $\delta = \sqrt{gD}/fL$ in (2.1) is the ratio of the deformation radius $\sqrt{gD}/f$ to the length scale of the flow L (or equivalently the cross-channel to the along-channel velocity scales). In the limit $\delta \to 0$ the acceleration terms in (2.1) can be neglected and v becomes geostrophically balanced. The resulting semigeostrophic equations remain hyperbolic and can be solved using the method of characteristics. In our dam break problem we may think of L as being the distance along the channel bottom between the leading edge of the intrusion, which moves towards positive y, and the leading edge of the transient that moves towards negative y. According to this definition L steadily increases from zero at $t = 0$ and thus the semigeostrophic approximation will be formally valid only after L becomes $\gg w$. For narrow channels the constraining effects of the sidewalls should suppress large u velocities and v should become geostrophic soon after the dam is removed. For wide channels a significant u velocity will develop in the central portion of the channel shortly after the dam

breaks. Both features are confirmed by comparison of the semigeostrophic solution with numerical solutions to the full shallow water equations (2.1)–(2.3).

In the limit $\delta \to 0$, the potential vorticity (2.5) is approximately $q = (1 + \partial v / \partial x)/d$. Combining this result with the geostrophic relation for v gives

$$\frac{\partial^2 d}{\partial x^2} - qd = -1. \tag{2.10}$$

For initial conditions (2.6)–(2.8) the potential vorticity q is a constant.

Following Gill (1977) it is convenient to write the solution to (2.10) for d, and hence v through geostrophy, as

$$d(x, y, t) = q^{-1} + \hat{d}(y, t)\frac{\sinh [q^{1/2}x]}{\sinh [\frac{1}{2}q^{1/2}w]} + (\bar{d}(y, t) - q^{-1})\frac{\cosh [q^{1/2}x]}{\cosh [\frac{1}{2}q^{1/2}w]}, \tag{2.11}$$

$$v(x, y, t) = q^{1/2}\hat{d}(y, t)\frac{\cosh [q^{1/2}x]}{\sinh [\frac{1}{2}q^{1/2}w]} + q^{1/2}(\bar{d}(y, t) - q^{-1})\frac{\sinh [q^{1/2}x]}{\cosh [\frac{1}{2}q^{1/2}w]}. \tag{2.12}$$

Here

$$\bar{d} \equiv \tfrac{1}{2}\left(d(w/2, y, t) + d(-w/2, y, t)\right) \tag{2.13}$$

is the average of the sidewall depths and

$$\hat{d} \equiv \tfrac{1}{2}\left(d(w/2, y, t) - d(-w/2, y, t)\right) \tag{2.14}$$

is half the difference in the sidewall depths. The cross-channel velocity $u(x, y, t)$ may be obtained diagnostically from (2.2) once d and v are known.

For the problem at hand the current may separate from the wall at $x = -w/2$. The fluid depth is then non-zero only over $w/2 - w_e < x < w/2$, where $w_e(y, t)$ is the width of the separated flow. The expressions for d and v then become

$$d(x, y, t) = q^{-1} + \bar{d}(y, t)\frac{\sinh [q^{1/2}(x - x_c(y, t))]}{\sinh [\frac{1}{2}q^{1/2}w_e(y, t)]} + (\bar{d}(y, t) - q^{-1})\frac{\cosh [q^{1/2}(x - x_c(y, t))]}{\cosh (\frac{1}{2}q^{1/2}w_e(y, t))} \tag{2.15}$$

$$v(x, y, t) = q^{1/2}\bar{d}(y, t)\frac{\cosh [q^{1/2}(x - x_c(y, t))]}{\sinh [\frac{1}{2}q^{1/2}w_e(y, t)]} + q^{1/2}(\bar{d}(y, t) - q^{-1})\frac{\sinh [q^{1/2}(x - x_c(y, t))]}{\cosh [\frac{1}{2}q^{1/2}w_e(y, t)]} \tag{2.16}$$

where $x_c = w - w_e(y, t)/2$. The two unknowns are now $\bar{d}$ and w_e.

The governing equations for $\bar{d}$ and $\hat{d}$ in the case of attached flow are found by applying (2.2) along the channel walls where $u = 0$ and substituting in the expressions (2.11)–(2.12) for d and v. This leads to (Pratt 1983)

$$q^{1/2}T^{-1}\frac{\partial \hat{d}}{\partial t} + \frac{\partial \bar{B}}{\partial y} = 0 \tag{2.17}$$

$$2q^{-1/2}T\frac{\partial \bar{d}}{\partial t} + \frac{\partial Q}{\partial y} = 0. \tag{2.18}$$

Here $Q = 2\bar{d}\hat{d}$ is the volume flow rate, $\bar{B} = \frac{1}{2}q[T^{-2}\hat{d}^2 + T^2(\bar{d} - q^{-1})^2] + \bar{d}$ is the average of the Bernoulli function on the two sidewalls, and $T \equiv \tanh(w/2)$. The

initial conditions for attached flow, from (2.6)–(2.8), are

$$\hat{d}(y,0) = 0, \tag{2.19}$$

$$\bar{d}(y,0) = \begin{cases} 1, & y < 0 \\ 0, & y > 0. \end{cases} \tag{2.20}$$

In the case of separated flow (which develops for $t > 0$ near the leading edge of the intrusion) the governing equations for $\bar{d}$ and w_e are again found by applying (2.2) along the channel wall at $x = w/2$ and along the separation streamline at $x = x_c(y,t)$ and using the standard kinematic boundary condition. This yields (Pratt 1983)

$$\frac{\partial(q^{1/2}T_e^{-1}\bar{d})}{\partial t} - \frac{1}{2}\frac{\partial w_e}{\partial t} + \frac{\partial \bar{B}}{\partial y} = 0 \tag{2.21}$$

$$\frac{\partial(q^{1/2}T_e(\bar{d} - q^{-1}))}{\partial t} + \frac{1}{2}\frac{\partial w_e}{\partial t} + \frac{1}{2}q\frac{\partial Q}{\partial y} = 0. \tag{2.22}$$

Here $Q = 2\bar{d}^2$, $\bar{B} = \frac{1}{2}q[T_e^{-2}\bar{d}^2 + T_e^2(\bar{d} - q^{-1})^2] + \bar{d}$ and $T_e \equiv \tanh(w_e/2)$.

3. Solution to the semigeostrophic initial value problem

3.1. *Overview*

The semigeostrophic solution is constructed using the method of characteristics. This type of analysis requires anticipation of the general aspects of the flow evolution and we are guided here by the known solution to the non-rotating version of the dam break problem (Stoker 1957). When the fluid depth downstream of the barrier ($y > 0$) is zero, the destruction of the barrier results in the formation of an intrusion, the leading edge or 'nose' of which moves towards positive y at speed $c_{nose} = 2$ (or twice the linear long gravity wave speed based on the initial depth behind the barrier). A second, backwards travelling propagating wave of depression is also generated and this wave moves upstream at the linear speed $dy/dt = c_l$ ($= -1$ non-dimensionally). The paths of these disturbances are shown by the thick lines in the (y,t)-plane of figure 1(a). As y varies from $c_l t$ to $c_{nose}t$, d continuously decreases and thus the intrusion consists of a spreading (or 'rarefying') region. In the case of non-zero initial depth in $y > 0$, the upstream portion of the disturbance is qualitatively unchanged from above, but the leading edge is replaced by a bore moving at positive speed c_{bore} (figure 1b). The region $c_l t < y < c_{bore}t$ is still one of spreading, though a portion of the flow just upstream of the bore has uniform d and v. We anticipate that the rotating versions of these flows will evolve in a similar manner, at least for sufficiently weak rotation. Verification of this expectation and generalization to strong rotation lies largely in the calculation of the speeds of the various transients as discussed shortly.

For the case of zero initial depth in $y > 0$, rotation can be expected to lead to one unavoidable complication, namely the separation of the flow from one of the sidewalls. For positive (northern hemisphere) rotation separation can be expected to occur first along the 'left' wall ($x = -w/2$) near the nose of the intrusion where the fluid depth is small. The separated region will extend from the nose $y = c_{nose}t$ upstream to a point $y = c_{sep}t$, as suggested in figure 1(a). Within this region, the semigeostrophic dependent variables are $\bar{d}(y,t)$ and $w_e(y,t)$. In the region $c_{sep}t > y > c_l t$ flow is attached and the dependent variables are $\bar{d}(y,t)$ and $\hat{d}(y,t)$.

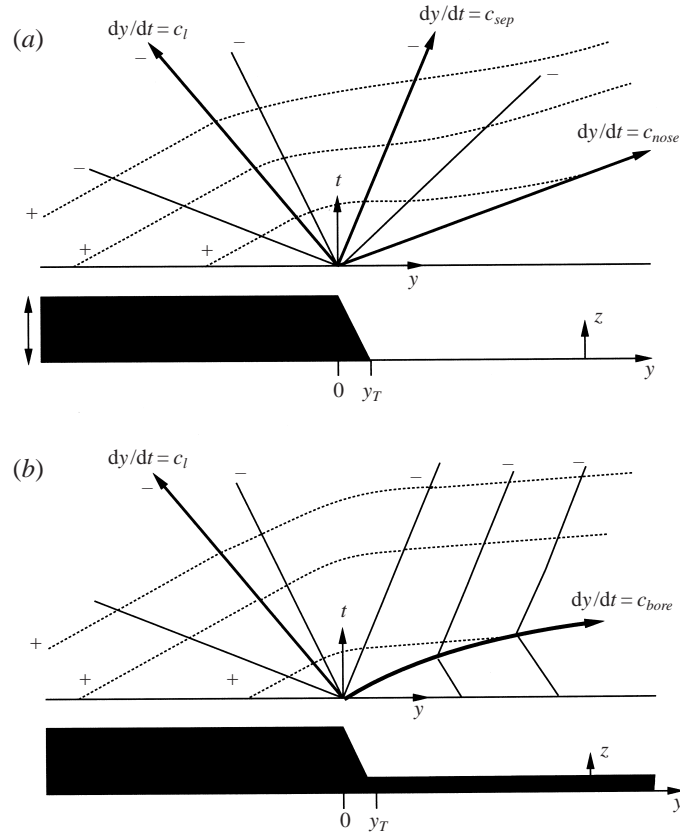The reader might wonder whether it is possible for the flow to separate in the

FIGURE 1. Sketch of characteristics in the (y, t)-plane for (a) zero upstream depth and (b) finite upstream depth. The thick solid lines indicate those special characteristic curves associated with the upstream wave ($dy/dt = c_l$), separation point ($dy/dt = c_{sep}$), the intrusion nose ($dy/dt = c_{nose}$) and the bore ($dy/dt = c_{bore}$). The thin solid lines indicate other negative characteristics and the dashed lines indicate positive characteristics. Below each characteristic sketch is a diagram indicating the initial depth of the fluid.

interior of the channel and yet remain attached to both sidewalls, which would lead to other possible regimes than shown in figure 1. In the limit of semigeostrophic motion, this complication can be ruled out by noting a theorem due to Gill (1977) which was originally derived for steady flow but is easily extended to our time-dependent problem. (Suppose that the flow at a given section begins to separate at an interior point x_0, meaning that d is non-zero for all other x at that section. Further assume that $\partial^2 d / \partial x^2$ exists at x_0 so that, clearly, $\partial^2 d / \partial x^2 > 0$ there. Then equation (2.10) is violated at x_0.) When the dynamics are non-semigeostrophic, there is no guarantee that interior separation will not occur. However, our numerical simulations will show that this type of separation does not occur in the dam break problem.

3.2. *Attached region*

The flow in the attached region is found using the method of characteristics to solve (2.17)–(2.18) with initial conditions (2.19)–(2.20). As long as $\bar{d} > \hat{d}$, the attached flow equations remain valid. When $\bar{d} = \hat{d}$, the flow is on the verge of separating and we must turn to the equations governing separated flow which are discussed in the next section.

Equations (2.17)–(2.18) are first put into standard quasi-linear form

$$\boldsymbol{u}_t + \boldsymbol{A}\boldsymbol{u}_y = 0 \tag{3.1}$$

with

$$\boldsymbol{u} = \begin{pmatrix} \bar{d} \\ \hat{d} \end{pmatrix}$$

and

$$\boldsymbol{A} = \begin{pmatrix} q^{1/2}\hat{d}T^{-1} & q^{1/2}\bar{d}T^{-1} \\ q^{1/2}T^3(\bar{d} - q^{-1}) + q^{-1/2}T & q^{1/2}\hat{d}T^{-1} \end{pmatrix}.$$

Diagonalization of (3.1) yields the interpretation that on the characteristic curves ('characteristics')

$$\frac{\mathrm{d}y}{\mathrm{d}t} = c_{\pm}^{attach} \equiv q^{1/2}\hat{d}T^{-1} \pm \bar{d}^{1/2}[1 - (1 - q\bar{d})T^2]^{1/2} \tag{3.2}$$

the relationship

$$\frac{\mathrm{d}\hat{d}}{\mathrm{d}\bar{d}} = \mp(q\bar{d})^{-1/2}T[1 - (1 - q\bar{d})T^2]^{1/2} \tag{3.3}$$

must hold. This second equation may be integrated to give

$$R_{\pm} = q^{1/2}\hat{d}T^{-1}$$
$$\pm\left(\bar{d}^{1/2}[1 - (1 - q\bar{d})T^2]^{1/2} + \frac{(1 - T^2)}{q^{1/2}T}\log\left[2(q\bar{d})^{1/2}T + 2[1 - (1 - q\bar{d})T^2]^{1/2}\right]\right) \tag{3.4}$$

where the Riemann invariants R_+ and R_- are constants of integration. The characteristic curves $\mathrm{d}y/\mathrm{d}t = c_{\pm}$ are indicated by the $+$ or $-$ in the (y, t)-planes shown in figure 1.

The Riemann invariants are conserved along characteristic curves and their values in the problem at hand are determined by the initial conditions in $x < 0$. Since the value of potential vorticity of a fluid column equals its initial reservoir value $q = 1/d(x, y, 0) = 1$, we set $q = 1$ in (3.4). With $\bar{d}(x, 0) = 1$ and $\hat{d}(x, 0) = 0$ the constants $R_{\pm}$ are now given by

$$R_{\pm} = \pm\left[1 + \left(\frac{1 - T^2}{T}\right)\log(2T + 2)\right]. \tag{3.5}$$

As posed, the solution to the dam break problem is non-unique. Different solutions can be found depending upon how one deals with the discontinuity in initial depth at $y = 0$. A reasonable way of thinking about the problem is to replace the discontinuity at $y = 0$ with the smooth, but abrupt, transition over $0 < y < y_T$ as shown in figure 1(a). The evolution resulting from this modified initial condition can be evaluated by calculating the Riemann invariants from the initial conditions and conserving these values along characteristic curves, at least until such time as a shock forms. Figure 1(a) shows the characteristic curves in the (y, t)-plane over a short time interval after the initial release. As in the non-rotating version of the dam break problem (Stoker 1957) analytical evaluation of the solution is greatly facilitated if one of the Riemann invariants is uniform. Clearly, both R_+ and R_- have the uniform values given by (3.5) over all characteristics emanating from the

constant-depth initial region ($y < 0$). If we choose R_-, say, to have the same uniform value in the transitional region ($0 < y < y_T$) then (3.4) can be used to show that the initial value of $\hat{d}$ must be less than zero there. Since $\hat{d}$ is proportional to the average of the wall values of v (which can be easily be obtained from (2.12)) the tendency will be for the leading edge of the intrusion to move towards negative y, which is inconsistent with our physical expectation. If we instead choose R_+ to be uniform over the transitional region then the average v is positive as desired. This choice is consistent with the solution to the non-rotating dam break problem, and with our numerical results.†

Once it has been established that R_+ is uniform over all parts of the domain (or at least those parts reached by non-intersecting 'plus' characteristic curves) it is easy to show that the values of the two dependent variables ($\bar{d}$ and $\hat{d}$) must be constant along 'minus' characteristics. (The uniformity of R_+ establishes a fixed relation between $\bar{d}$ and $\hat{d}$ which holds at all points throughout the domain. The conservation of R_- along 'minus' characteristics imposes an independent relation along each such curve. Satisfaction of both constraints is only possible if *both* $\bar{d}$ and $\hat{d}$ remain fixed along each such curve.) Thus c_- must also be conserved along 'minus' characteristics, implying that these curves have constant slope in the characteristic plane. As we will confirm by direct calculation the values of c_- along characteristics emanating from the forward (smaller depth) portion of the transitional region are larger than those from the rear, so that the 'minus' characteristics fan out as shown in figure 1(*a*). The leading 'minus' characteristic has $\bar{d} = \hat{d} = 0$ and defines the nose. (This curve is also a 'plus' characteristic.) The separation point ($\bar{d} = \hat{d} \neq 0$) also occurs along a 'minus' characteristic. Between these last two lines, the Riemann invariants for separated flow (§3.3) must be used. The leading edge of the signal propagating back into the stationary fluid has $\hat{d} = 0$ and $\bar{d} = 1$ and this is a 'minus' characteristic as well. The 'plus' characteristics emanating from ($y < 0$) are straight until they penetrate the region of fanning 'minus' characteristics where they curve and eventually become tangent to the 'minus' characteristic defining the nose.

When the initial depth in $y > 0$ is non-zero the situation is as shown in figure 1(*b*). These fanning characteristics are intersected by straight 'minus' characteristics emanating from $y > 0$, creating a shock, or bore. The path of the bore is indicated by the solid, curved arrow in figure 1(*b*). The shallow water equations break down within the bore and additional considerations are required to determine its speed c_{bore}. In the non-rotating version of this problem, c_{bore} can be determined by imposing bulk mass and momentum conservation, but rotation leads to additional difficulties which will be discussed in §5. For this reason, our solution for this case is entirely numerical.

---

† The question of uniqueness in the dam break problem also arises in connection with a reduced-gravity, coastal version of the dam break problem considered by Stern *et al.* (1982). They found a similarity solution for a steepening intrusion (a bore) advancing along a coastline. Their solution essentially has uniform values of R_-, in contrast with our solution. There are several differences between the two problems which are worth noting. First, their solution was motivated by results of a laboratory experiment in a two-fluid system in which the advancing intrusion steepens and forms a blunt nose, which is quite different from the spreading nose which we will demonstrate in connection with the present single-layer problem. In addition, Stern *et al.* (1982) do not solve the complete initial-value problem in the way we do. In fact, a complete solution for the case simulated in their experiment would be considerably complicated by reflections off the endwalls in their laboratory tank.

Returning to the original dam break problem (figure 1*a*) the values of $\bar{d}$ and $\hat{d}$ in the attached region of the characteristic fan are obtained as follows. The characteristic speeds (inverse slopes of the characteristics) are given by

$$y/t = \hat{d}T^{-1} - \bar{d}^{1/2}[1 - (1 - \bar{d})T^2]^{1/2}. \tag{3.6}$$

Setting $\hat{d} = 0$ and $\bar{d} = 1$ in this equation gives the speed $y/t = c_l = -1$. This is simply the speed of a linear Kelvin wave propagating into the region $y < 0$. When the channel is wide $w \gg 1$ this wave is trapped at the left ($x = -w/2$) wall. The other constraint used in the region of attached flow is the uniformity of R_+ which implies

$$1 + \left(\frac{1 - T^2}{T}\right)\log(2T + 2) = \hat{d}T^{-1} + \bar{d}^{1/2}[1 - (1 - \bar{d})T^2]^{1/2}$$

$$+ \frac{(1 - T^2)}{T}\log[2\bar{d}^{1/2}T + 2[1 - (1 - \bar{d})T^2]^{1/2}]. \tag{3.7}$$

To find $y/t = c_{sep}$ set $\hat{d} = \bar{d}$ and eliminate $\bar{d}$ from the above two equations (which must be done numerically). The solutions for $\bar{d}$ and c_{sep} are discussed §4. A qualitative description of their dependence on T can be found by examining the narrow and wide channel limits. For the narrow channel, setting $T = 0$ in (3.7) gives $\bar{d}_{sep} = 0$. In this limit the two-dimensional nature of the flow caused by rotation is suppressed and the point of flow separation on the left-hand wall coincides with the intrusive nose on the right-hand wall. The speed of the separation point c_{sep} as a function of T is found by solving (3.6) with $\bar{d} = \hat{d} = \bar{d}_{sep}$ and $y/t = c_{sep}$. This yields the dependence of c_{sep} on $\bar{d}_{sep}$. In the narrow channel limit, $\bar{d}_{sep} = 0$, which gives $c_{sep} = 2$. This agrees, as expected, with the non-rotating solution (Stoker 1957). In the wide channel limit, $T = 1$, giving $\bar{d}_{sep} = 0.5$ from (3.7) and $c_{sep} = 0$ from (3.6). In this case the separation point remains at the position of the dam and the value of d along the right-hand wall remains equal to the initial depth, $d = 1$.

3.3. *Solution: separated region*

The solution in the separated region is also obtained by the method of characteristics. As before, (2.21) and (2.22) are cast into standard quasi-linear form

$$\boldsymbol{v}_t + \boldsymbol{B}\boldsymbol{v}_y = \boldsymbol{0} \tag{3.8}$$

where

$$\boldsymbol{v} = \begin{pmatrix} \bar{d} \\ T_e \end{pmatrix}$$

and

$$\boldsymbol{B} = \begin{pmatrix} \dfrac{3q\bar{d} + T_e^2 + (q\bar{d} - 1)T_e^4}{2q^{1/2}T_e} & \dfrac{(q\bar{d} - 1)^2 T_e^4 - (q\bar{d})^2}{2q^{3/2}T_e^2} \\[4mm] \dfrac{q^{1/2}(T_e^2 - 1)^2(q\bar{d} - (1 - q\bar{d})T_e^2}{2(q\bar{d} + (1 - q\bar{d})T_e^2)} & \dfrac{(1 - T_e^2)(q\bar{d} - (1 - q\bar{d})T_e^2)}{2q^{1/2}T_e} \end{pmatrix}.$$

Multiplication of (3.8) by the left eigenvector matrix $\boldsymbol{S}^{-1}$ of $\boldsymbol{B}$ yields

$$\boldsymbol{S}^{-1}\boldsymbol{v}_t + \boldsymbol{\Lambda}\boldsymbol{S}^{-1}\boldsymbol{v}_y = \boldsymbol{0}. \tag{3.9}$$

The elements of $\mathbf{S}^{-1}$, $\hat{s}_{ij}$, are

$$\hat{s}_{11} = \frac{1}{\det \mathbf{S}},$$

$$\hat{s}_{12} = \frac{1}{\det \mathbf{S}} \left(\frac{-q^2\bar{d}^2 + (1 - 2q\bar{d} + q^2\bar{d}^2)T_e^4}{qT_e\left(q\bar{d} + T_e^2 + (q\bar{d} - 1)T_e^4 + 2(q\bar{d})^{1/2}T_e[1 - (q\bar{d} - 1)T_e^2]^{1/2}\right)} \right),$$

$$\hat{s}_{21} = -\hat{s}_{11},$$

$$\hat{s}_{22} = \frac{1}{\det \mathbf{S}} \left(\frac{q^2\bar{d}^2 - (1 - 2q\bar{d} + q^2\bar{d}^2)T_e^4}{qT_e\left(q\bar{d} + T_e^2 + (q\bar{d} - 1)T_e^4 - 2(q\bar{d})^{1/2}T_e[1 - (q\bar{d} - 1)T_e^2]^{1/2}\right)} \right).$$

The diagonal matrix Λ is given by

$$\Lambda = \begin{pmatrix} c_+^{sep} & 0 \\ 0 & c_-^{sep} \end{pmatrix},$$

where

$$c_\pm^{sep} = q^{1/2}\bar{d}T_e^{-1} \pm \bar{d}^{1/2}[1 - (1 - q\bar{d})T_e^2]^{1/2}. \tag{3.10}$$

Note that (3.10) is just (3.2) with $\hat{d}$ replaced by $\bar{d}$ and T replaced by T_e.

Equation (3.9) implies two differential relationships between $\bar{d}$ and T_e (corresponding to the plus and minus Riemann invariants),

$$\frac{\mathrm{d}T_e}{\mathrm{d}\bar{d}} = -\frac{\hat{s}_{11}}{\hat{s}_{12}} = \frac{qT_e\left(q\bar{d} + T_e^2 + (q\bar{d} - 1)T_e^4 + 2(q\bar{d})^{1/2}T_e[1 - (q\bar{d} - 1)T_e^2]^{1/2}\right)}{q^2\bar{d}^2 - (1 - 2q\bar{d} + q^2\bar{d}^2)T_e^4}, \tag{3.11}$$

$$\frac{\mathrm{d}T_e}{\mathrm{d}\bar{d}} = -\frac{\hat{s}_{21}}{\hat{s}_{22}} = \frac{qT_e\left(q\bar{d} + T_e^2 + (q\bar{d} - 1)T_e^4 - 2(q\bar{d})^{1/2}T_e[1 - (q\bar{d} - 1)T_e^2]^{1/2}\right)}{q^2\bar{d}^2 - (1 - 2q\bar{d} + q^2\bar{d}^2)T_e^4}, \tag{3.12}$$

which must hold on the characteristic lines $\mathrm{d}y/\mathrm{d}t = c_\pm^{sep}$.

Were we able to solve (3.11) and (3.12) analytically, the constants of integration would yield the two Riemann constants.† Then $\bar{d}$ and T_e could be found by the simultaneous solution of (3.11), (3.12) and the straight characteristic $y/t = c_-^{sep}$. However, (3.11) and (3.12) must be integrated numerically. The solution for $\bar{d}$ is assumed to be continuous across the line $y/t = c_{sep}$ shown in figure 1(*a*). The integration is started with $\bar{d} = \bar{d}_{sep}$ and $T_e = T$ and stepped backward in $\bar{d}$ until $\bar{d}$ is $O(10^{-6})$ which is identified at the nose of the intrusion.

Evaluation of T_e versus $\bar{d}$ on the 'plus' Riemann invariant (the integral curve of (3.11)) shows that $T_e \to 0$ as $\bar{d} \to 0$ for all w. The nose of the separated region not only has zero height, as might be expected, but also has zero width. It can be shown that near the nose, $w_e \approx \bar{d}$ in the narrow channel limit $T \to 0$, and $w_e \approx 2\bar{d}$ in the wide channel limit $T \to 1$.

With T_e obtained numerically as a function of $\bar{d}$, it is a simple matter to solve for those variables separately as functions of the similarity variable y/t on the 'minus' characteristic $y/t = c_-^{sep}(\bar{d}, T_e)$.

---

† We note that figures showing contours of the Riemann invariants appear in Stern *et al.* (1982) and Kubokawa & Hanawa (1984*a*).
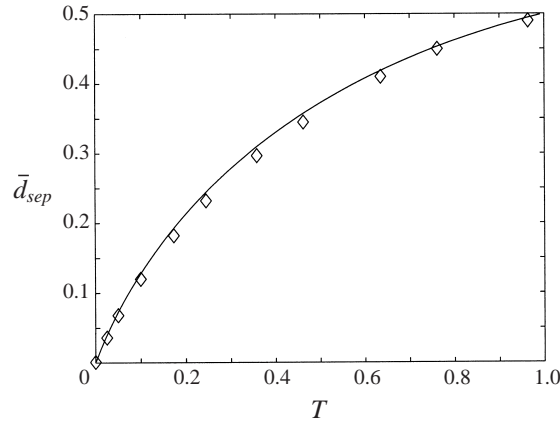
FIGURE 2. $\bar{d}_{sep}$ versus $T = \tanh(w/2)$. The solid line is the semigeostrophic theory. In this and subsequent figures the symbols indicate results from the numerical model. For reference $T = 0.462$ for $w = 1$ and $T = 0.96$ for $w = 4$.

4. Semigeostrophic and full numerical solutions

In this section solutions from the semigeostrophic theory are presented and compared with the results from numerical solutions. The numerical model solves the shallow water equations, (2.1)–(2.3) with $\delta = 1$, in conservative form. The use of the conservative form of the equations is not required for the pure rarefaction waves that are discussed in this section, but is necessary if shocks are to be accurately resolved. This latter situation, discussed in §5, arises when the fluid downstream of the dam has a finite initial depth. Details of the numerical model are given in the Appendix. The model allows nearly zero layer depth (limited to a minimum of 10^{-10}). In what follows we define the edge of the evolving intrusion in the full numerical solutions (e.g. nose, separation point) to be where the layer depth equals 10^{-3}. This choice is arbitrary, but the results are not sensitive to this definition.

Figure 2 shows the value of $\bar{d}$ at the separation point, $\bar{d}_{sep}$, as a function of the width parameter T. In this and subsequent figures in this section the semigeostrophic theory is indicated by lines and the numerical model results by the symbols, unless otherwise stated. The data points from the numerical model were obtained by extrapolating the cell-centred values of d in the two cells adjacent to each channel wall. In the limit of zero channel width $\bar{d}_{sep} \to 0$ and as $T \to 1$, $\bar{d}_{sep} \to 0.5$, as previously discussed. The agreement between the numerical model and the semigeostrophic theory is quite good for all widths. One difference between the theory and the full shallow water equations not evident in this figure are transverse oscillations. These are illustrated in figure 7 and discussed later.

The speeds of the separation point c_{sep} and nose of the intrusion c_{nose} as functions of T are shown in figure 3. The upper solid curve is c_{nose} determined from (3.10) and the Riemann invariant from (3.11) with the nose defined to have a depth $d = 10^{-6}$. The three curves below this one are c_{nose} defined with $d = 10^{-5}$, 10^{-4} and 10^{-3}. The speeds converge and support our use of $d = 10^{-6}$ to define the nose. The lower solid curve is c_{sep} determined from (3.6) and (3.7). The semigeostrophic theory gives $c_{sep} = c_{nose} = 2$ for $T = 0$, in agreement with the non-rotating solution. As the channel width increases c_{nose} (c_{sep}) increases (decreases) monotonically. For an infinitely wide channel $c_{nose} = 3.80$ and, as already noted, $c_{sep} = 0$.
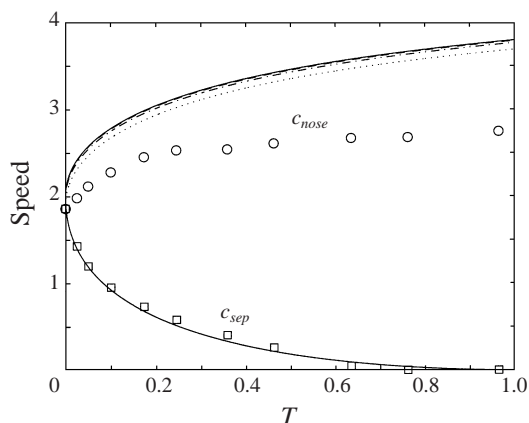
FIGURE 3. The intrusion nose speed c_{nose} and the separation point speed c_{sep} as functions of the width parameter T. The upper solid line is the semigeostrophic solution for c_{nose} defined at a depth of $d = 10^{-6}$. The broken lines are c_{nose} defined with $d = 10^{-5}$ (dashed), 10^{-4} (dash-dot) and 10^{-3} (dotted). The lower solid line is c_{sep} from the semigeostrophic theory. The circles and squares are the numerical model results for c_{nose} and c_{sep}, respectively.

The numerical model solutions for c_{nose} (defined with $d = 10^{-3}$) are shown in figure 3. They are significantly less than the semigeostrophic theory. The agreement with the theoretical speed for a nose depth of $d = 10^{-3}$ is not much better. It is difficult to attribute this discrepancy to a failure of the semigeostrophic theory. Indeed, the nose region is one of large along-channel length scales where, as discussed earlier, the semigeostrophic approximation is expected to be valid. The theory predicts an ever-thinning nose which the numerics can never follow accurately with fixed grid resolution. We attribute most of the the differences in c_{nose} to the finite resolution of the numerical grid and lateral viscosity (numerical and explicit), neither of which are present in the theory.

The numerical model values for c_{sep} shown in figure 3 do agree quite well with the semigeostrophic solution. The separation point does not suffer from the worst of the numerical resolution issues affecting the intrusion nose. In the model results the separation point motion is affected by cross-channel oscillations, particularly for channels with $w \gtrsim 2$. The speeds plotted in figure 3 are determined from the mean motion of the separation positions. The intrusion nose is unaffected.

The semigeostrophic solution for $\bar{d}$, $\hat{d}$ and T_e is plotted in figure 4 as a function of the similarity variable y/t for four values of w. At the separation point ($\bar{d} = \hat{d}$) $\partial \bar{d}/\partial y$ is discontinuous, indicating that the semigeostrophic approximation is suspect in this neighbourhood.

Next, we compare the depth field $d(x, y, t)$ from semigeostrophic theory and the numerical model. Solutions are shown at $t = 10$ for two channel widths, $w = 0.2$ in figure 5 and $w = 2.0$ in figure 6. The semigeostrophic solution is in panel (*a*), the numerical solution is in (*b*). For $w = 0.2$, the two solutions agree quite well everywhere except in the immediate vicinity of the intrusion nose where the numerical model under-resolution is obvious. When $w = 2.0$, the overall character of the full solution is reproduced by the semigeostrophic theory, but there are some areas of disagreement, particularly in the centre of the channel near the separation point. The differences in the separation zone are to be expected, since the acceleration of the cross-channel component of the velocity u, neglected in the semigeostrophic theory, is large.
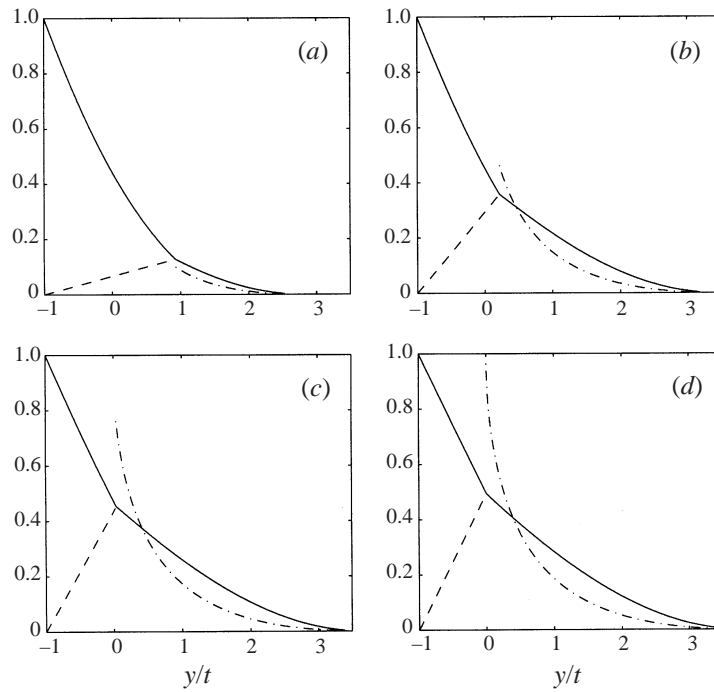
FIGURE 4. Semigeostrophic solutions for (*a*) $w = 0.2$, (*b*) 1, (*c*) 2 and (*d*) 4. Each plot shows $\bar{d}$ (solid line), $\hat{d}$ (dashed line) and T_e (dash-dot line) as functions of the similarity variable y/t.
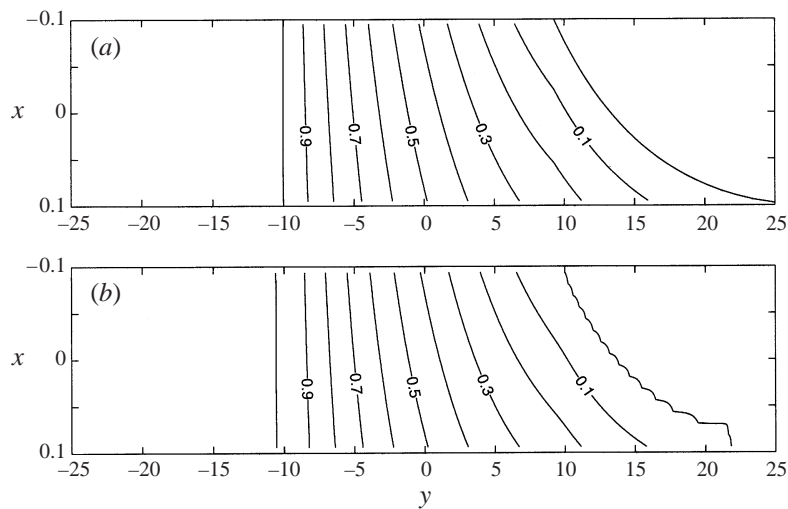

FIGURE 5. Contours of the depth d field at $t = 10$ for a channel with $w = 0.2$. (*a*) The semigeostrophic solution. (*b*) The numerical solution to the full shallow water equations. The contours interval is 0.1.

The breakdown of the semigeostrophic theory for a wide channel is illustrated in figure 7, which shows the evolution in time of the depth field from a numerical solution with $w = 4$. Immediately after the dam is removed ($t = 2$) a shock-like feature develops near the right-hand wall at $(x, y) = (2, 1)$. It propagates across the channel ($t = 4$ and 6) and is followed by another, weaker, large-gradient region
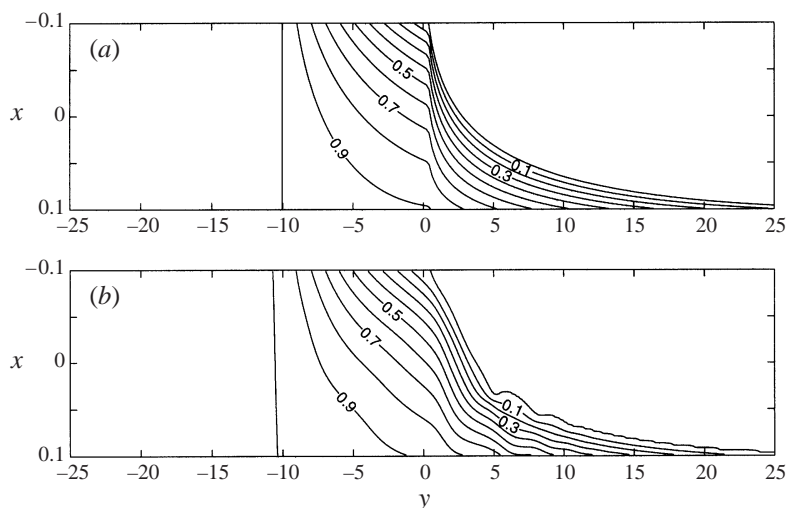
FIGURE 6. Same as figure 5 except $w = 2$.

slightly downstream ($t = 6, 8$ and 10). The large gradients in d and associated large accelerations in u violate the semigeostrophic assumption. The cross-channel disturbances affect the structure of the intrusive tongue leading to the formation of bulges which propagate downstream. However the nose of the intrusion is unaffected. The severity of the cross-channel motion, and consequently the error induced by using the semigeostrophic approximation, increases with channel width, but becomes significant only for $w \gtrsim 2$.

4.1. *Asymptotic flow*

Despite the limitations of the semigeostrophic approximation, many aspects of the flow are captured by the theory (e.g. $\bar{d}_{sep}$ and c_{sep}). This is particularly true for long times as the effects of cross-channel motions decrease and the along-channel scales become large. Here we examine the long time nature of the flow at any fixed position y along the channel as $t \to \infty$. Since for all except an infinitely wide channel the separation point will eventually move downstream of any fixed y location, the flow will be attached and (3.6) and (3.7) are relevant. Because these equations are functions of y/t, the steady solution at any position y approaches the solution evaluated at $y = 0$ at any $t > 0$. As $t \to \infty$ the flow becomes y-independent and the flow approaches criticality.

Figure 8 shows the steady solutions for $\bar{d}$ and $\hat{d}$ as functions of T which are obtained from (3.6) and (3.7) with $y/t = 0$. The results from the numerical model at $y = 0$ are also shown. The numerical values are averages over several oscillation periods once the large initial transients have decayed. The inset shows an example of the temporal evolution of $\bar{d}$ and $\hat{d}$ at $y = 0$ from the numerical model for $w = 2$. Widths less that this exhibited faster convergence to the large-time values. The steady-state values of $\bar{d}$ in the limit $T \to 0$ from both the theory and numerical model agrees with the non-rotating solution $d = (2/3)^2 \approx 0.44$ (Stoker 1957). The agreement between the theory and numerical solution is quite good over the full range of T.

The asymptotic mass transport $Q = 2\bar{d}\hat{d}$ can also be readily calculated and is shown in figure 9 as a function of w. In the narrow channel limit the rotating solution should approach the non-rotating solution in which the depth and velocity
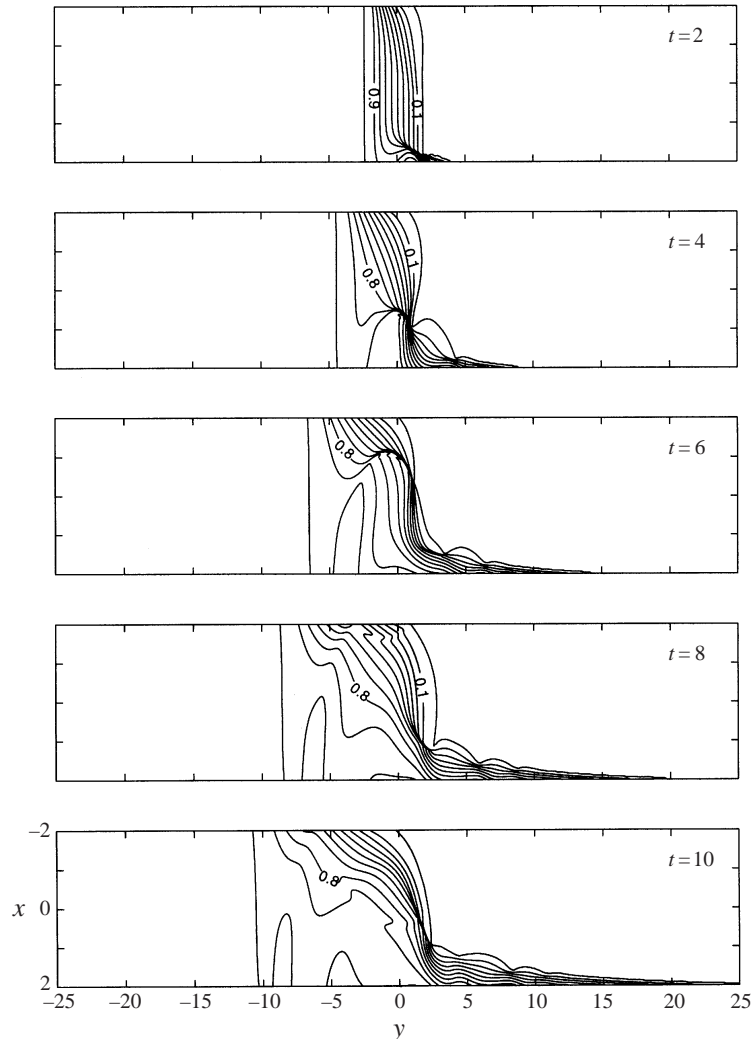
FIGURE 7. Full numerical solution for $d(x, y, t)$ at several indicated times for a channel of width 4. The contour interval is 0.1.

are constants independent of x and y. The transport is a linear function of width, $Q = dvw = (2/3)^3 w$. This line is shown in figure 9. Also shown are the average transport values from the numerical model. Channels with widths smaller than roughly a deformation radius agree with the non-rotating theory. Beyond about one deformation radius rotational influences reduce the transport below the non-rotating value. For very wide channels $Q \sim T/2$. In the infinite width limit the only length scale is the deformation radius. The transport then approaches a constant value of $1/2$. Again the theory and the numerical model are in good agreement.

We might also ask whether the transports shown are bounded by the value suggested by Toulany & Garrett (1994) in their discussion of 'geostrophic control'. According to this principle the steady volume transport between two rotating reservoirs cannot be greater than $gD\Delta z/f$, where Δz is the difference in surface elevation between the two reservoir interior depths and D is the mean depth of the system. The reservoirs
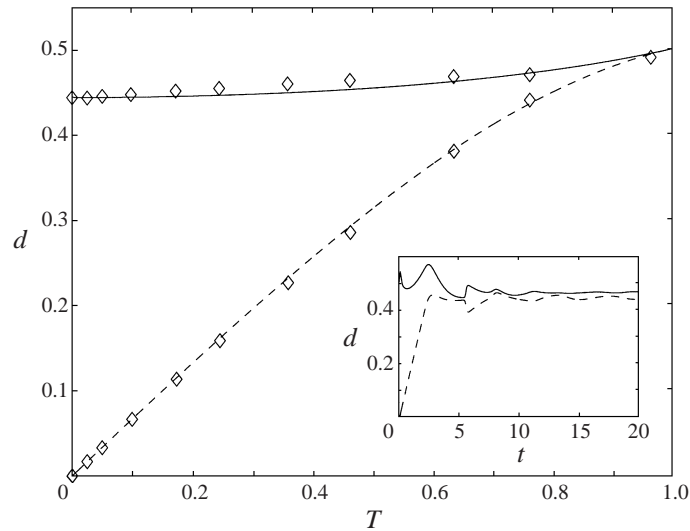
FIGURE 8. Asymptotic steady-state solution for $\bar{d}$ and $\hat{d}$ versus T. The solid (dashed) line is $\bar{d}$ ($\hat{d}$) from the semigeostrophic theory and the symbols are results from the numerical model. The inset shows $\bar{d}$ (solid) and $\hat{d}$ (dashed) at $y = 0$ as a function of t from the numerical solution for $w = 2$.
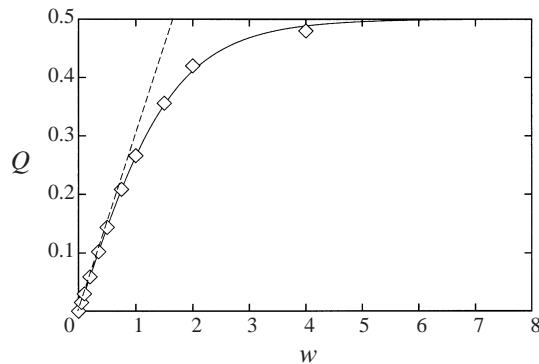

FIGURE 9. Steady-state transport Q versus w for the dam break problem. The solid line is the semigeostrophic theory, the dashed line is the non-rotating theory and the symbols are results from the numerical model.

are much wider than the Rossby radius of deformation, so that the throughflow is restricted to boundary layers and the surface elevation is uniform in the reservoir interiors. This linear bound was developed for systems with small elevation changes ($\Delta z \ll D$) but the generalization for arbitrary depth changes is $(g/2f)(d_u^2 - d_d^2)$, where d_u and d_d are the upstream and downstream reservoir depths, respectively. (In our non-dimensionalization it becomes $\frac{1}{2}(1 - d_0^2)$, where d_0 is the scaled downstream depth.) The bound is based on the anticipation that steady flow from the upstream reservoir will approach the connecting strait in a boundary layer along the left-hand wall, cross to the right-hand wall within the strait, and continue into the second reservoir as a boundary current along the right-hand wall. The above bound then follows from the geostrophic relation and the supposition that the depth difference across the boundary layer cannot be greater than $d_u - d_d$. In the dam break problem, we may regard the regions upstream and downstream as the two reservoirs, provided that the

channel width is a few deformation radii or more wide. If we then base d_u and d_d on the asymptotic ($t \to \infty$) flow, then the bound generally fails. (The asymptotic flow is uniform in y and therefore $d_u - d_d = 0$). The lone exception is the wide-channel limit ($T \to 1$), for which the separation point remains at $y = 0$ and the asymptotic flow switches sides as envisioned. The non-dimensional values of d_u and d_d for this case remain unchanged from their initial values (1 and 0), so that the bound ($= \frac{1}{2}$) exactly matches the actual transport. Also note that the actual transport for any finite w is always less than the bound ($= \frac{1}{2}$) obtained by interpreting d_u and d_d as the initial depths.

The reduction in transport by rotation is a feature anticipated by steady hydraulic theories such as Whitehead *et al.* (1974). However, this conclusion is typically reached by fixing the reservoir state upstream of a strait or sill and calculating the change in outflow rate as rotation is increased. There is no guarantee, of course, that the reservoir state should remain fixed as rotation increases. The results of our initial value problem would seem to avoid these ambiguities.

5. Finite downstream depth

When the initial fluid depth downstream of the dam d_0 is finite the rarefying intrusion is replaced by a Kelvin wave which proceeds along the right-hand wall. Linear theory is applicable when the difference in initial depths upstream and downstream of the dam, $1 - d_0$, is very small. When $1 - d_0$ is large the flow is fully nonlinear and analytical progress, even in the semigeostrophic limit, is difficult. This is due to the formation of a bore, or shock, at the leading edge of the disturbance that propagates downstream into the shallow layer. The non-rotating nonlinear problem can be solved analytically (Stoker 1957) since the conditions for joining the solution across the shock (mass and momentum flux conservation) are known. The presence of rotation leads to uncertainty in determining what conservation constraint, in addition to mass and momentum fluxes, must be imposed across the shock. In general, potential vorticity is not conserved across the shock (Pratt 1983; Nof 1986).

In this section we consider finite downstream depth and study the flow evolution beyond the linear and weakly nonlinear regimes. As in the previous sections we limit our effort to hydrostatic flow. Because of the complications associated with the full nonlinearity we approach the problem with a numerical model of the single-layer shallow water equations described in the Appendix. In addition to determining the effects of rotation on the overall evolution and bore characteristics we also examine the Lagrangian advection of fluid particles down the channel.

5.1. *General evolution*

Examples of the evolution of the depth field $d(x, y, t)$ as a function of w and d_0, the two independent parameters in the problem, are shown in figures 10–15. The initial conditions for all the results discussed in this section are given by (2.6)–(2.8), but with $d(x, y, 0) = d_0$ for $y > 0$. The figures show the contours of the depth field $d(x, y, t)$ at several times after removal of the dam.

A narrow channel example, $w = 0.5$, with $d_0 = 0.5$ is shown in figure 10. As expected the evolution of d is qualitatively the same as the non-rotating case (Stoker 1957). Immediately after the dam is removed a shock forms and propagates downstream. Propagating upstream ($y < 0$) is a rarefying Kelvin wave. Between the shock and the upstream moving Kelvin wave is an expanding region that is nearly uniform in y. This region is connected to the shock by a transition layer of several deformation radii
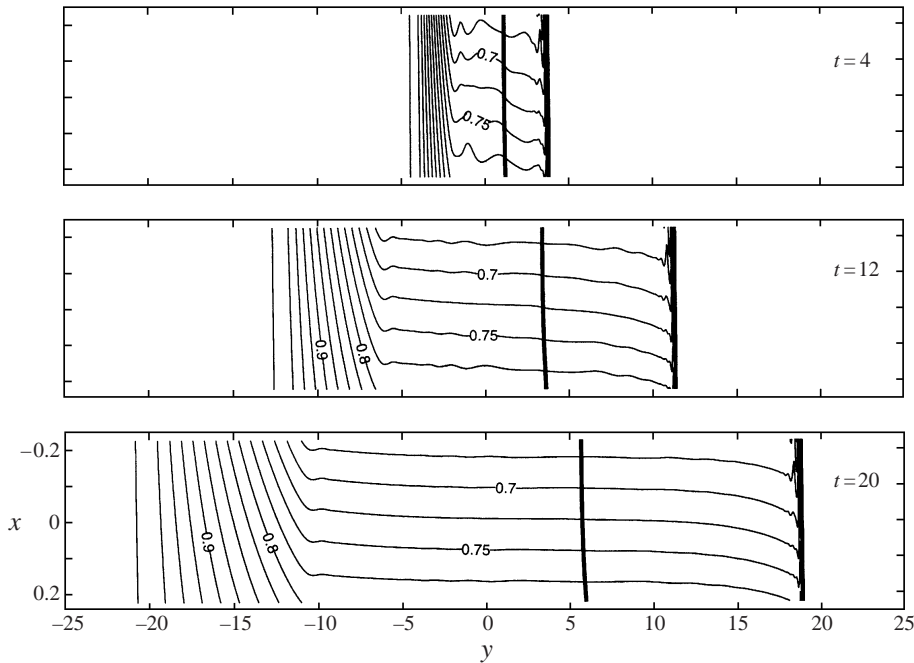
FIGURE 10. Numerical solution for $d(x, y, t)$ for finite downstream depth $d_0 = 0.5$ and $w = 0.5$. The contour interval is 0.025 with several contours marked. The thick solid line is the $c = 0.5$ contour identifying the interface between water originally upstream and downstream of the dam.

in length in which the depth decreases as the shock is approached from behind. The shock is oriented straight across the channel and propagates at a uniform speed and with very little change in shape. The very small-scale wiggles in the depth contours (e.g. $d = 0.75$ at $t = 20$) immediately behind the shock are due to numerical errors in resolving the discontinuity and are indicative of the magnitude of this effect in other runs. The larger oscillations near the left-hand wall are physical and are discussed in examples below. The shock amplitude (defined by the jump in height from the downstream level d_0 to the peak of the discontinuity, but not including the transition region) decreases away from the right-hand wall. Near the left-hand wall the leading edge of the shock is a thin, high ridge of fluid deeper than the fluid immediately behind it. The cross-channel component of velocity (not shown) is nearly zero everywhere except in a boundary layer of about one deformation radius in thickness immediately behind the shock. Further details of the shock structure are discussed in the following subsection.

Also shown in the figures (by the thick line) is the interface between fluid originally upstream of the dam and fluid downstream. This division is determined by numerical solution for the concentration c of a conservative tracer governed by

$$\frac{\partial c}{\partial t} + u \frac{\partial c}{\partial x} + v \frac{\partial c}{\partial y} = 0,$$

with initial conditions $c(x, y, 0) = 1$ for $y < 0$ and $c(x, y, 0) = 0$ for $y > 0$. Thus c serves as a proxy for the potential vorticity q, which would also be a materially conserved property in the absence of shocks and explicit dissipation. The motion of the discontinuity in c is analogous to the advection of the discontinuity in q studied by HRJ. The thick solid lines in figures 10–15 are the $c = 0.5$ contours which we

identify as the interface. The numerical model does result in some diffusion of the initially sharp discontinuity in c, but the thickness is usually less than one deformation radius. In figure 10 the interface moves nearly uniformly down the channel.

The evolution in a wider channel, $w = 1$, is shown for $d_0 = 0.5, 0.25$ and 0.05, in figures 11, 12 and 13, respectively. The solution for $d_0 = 0.5$ is qualitatively the same as figure 10 ($w = 0.5$) except that Poincaré waves are evident in the region between the shock and the upstream advancing rarefaction wave. The shock is still propagating steadily, but with a very slight curvature across the channel. Poincaré waves are also evident immediately behind the shock near the left-hand wall. These features are physical and not a consequence of dispersive numerical errors. The interface contour moves slightly faster on the right-hand wall than on the left, but still lags far behind the leading bore. The interface is also a location of cross-channel geostrophic flow indicated by the local along-channel gradient in d. This feature was not present in the narrower, $w = 0.5$, case in figure 10.

When the initial upstream depth is reduced to $d_0 = 0.25$ (figure 12) the oscillations immediately behind the shock are enhanced. The wavy region lengthens as the bore moves down the channel. We interpret this as a finite-amplitude example of resonant Poincaré wave generation by nonlinear Kelvin waves discussed by Melville *et al.* (1989). The apparent radiation of the waves behind the leading shock implicates the resonant mechanism as their source rather than initial transients. However, in these strongly nonlinear examples it proved difficult to predict the wavelength of the resonant Poincaré waves using the weakly nonlinear argument of Melville *et al.* (1989). The background state on which the waves propagate has non-uniform depth and velocity making determination of the dispersion relation non-trivial. Further, the large amplitude of the waves makes their description through linear dynamics tenuous. The $c = 0.5$ interface now defines a tongue of new fluid which advances preferentially along the right-hand wall, but at a speed still substantially less than the bore speed.

When the initial upstream depth is further reduced to $d_0 = 0.05$ (figure 13) the shock attaches only to the right-hand wall. It curves slightly back upstream and decays with distance from the wall. The Poincaré waves immediately behind the shock are nearly eliminated. Again propagation is steady once the shock has separated from the initial transients. The fluid interface moves much faster along the right-hand wall at a speed just slightly slower than the bore speed.

Two wide channel, $w = 4$, cases with $d_0 = 0.5$ and 0.1 are shown in figures 14 and 15, respectively. In figure 14 the upstream moving Kelvin wave and downstream propagating shock are both trapped near their respective right-hand walls with cross-channel decay scales of about one deformation radius based upon the initial upstream depth. Fluid crosses the channel near $y = 0$ in a nearly steady geostrophic current and advances along the right-hand wall. The $c = 0.5$ contour is advected slowly downstream across most of the channel except for a thin ribbon near the right-hand wall where it advances more rapidly. The interface advances slightly faster along the left-hand wall than in the centre of the channel. This feature was observed by HRJ in both contour dynamics calculations and solutions to the shallow water equations.

For $d_0 = 0.1$ (figure 15) the evolution is similar to $d_0 = 0.5$ except that the shock and its trailing current have further narrowed. The angle that the leading edge of the bore makes with the x-axis has also increased. At $t = 4$ a steep cross-channel propagating feature similar to the $d_0 = 0$ case in figure 7 is evident. The interface contour moves rapidly just behind the shock along the right-hand wall. However, as time increases the interface along the left-hand wall moves back upstream to $y < 0$.
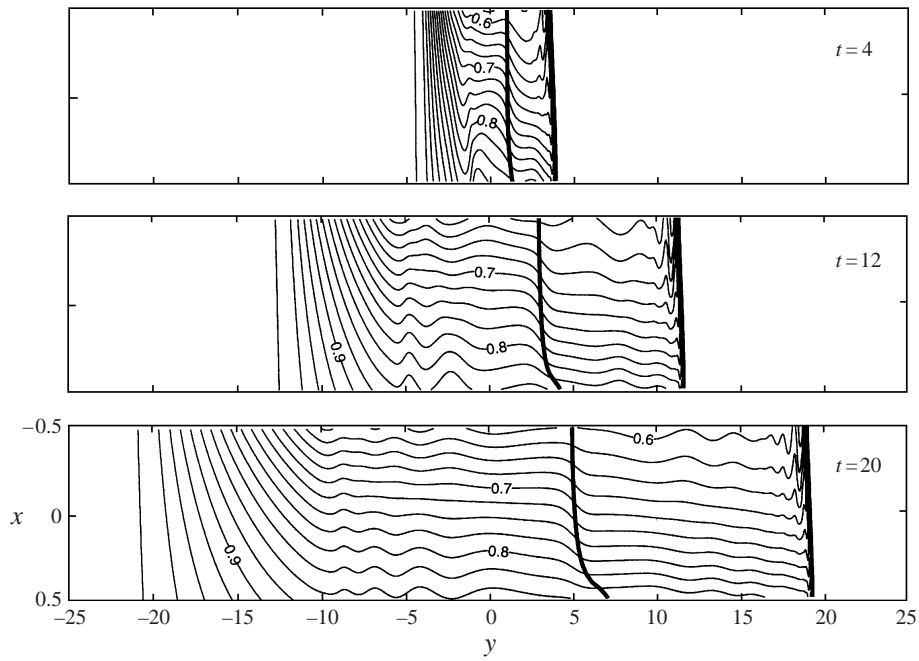
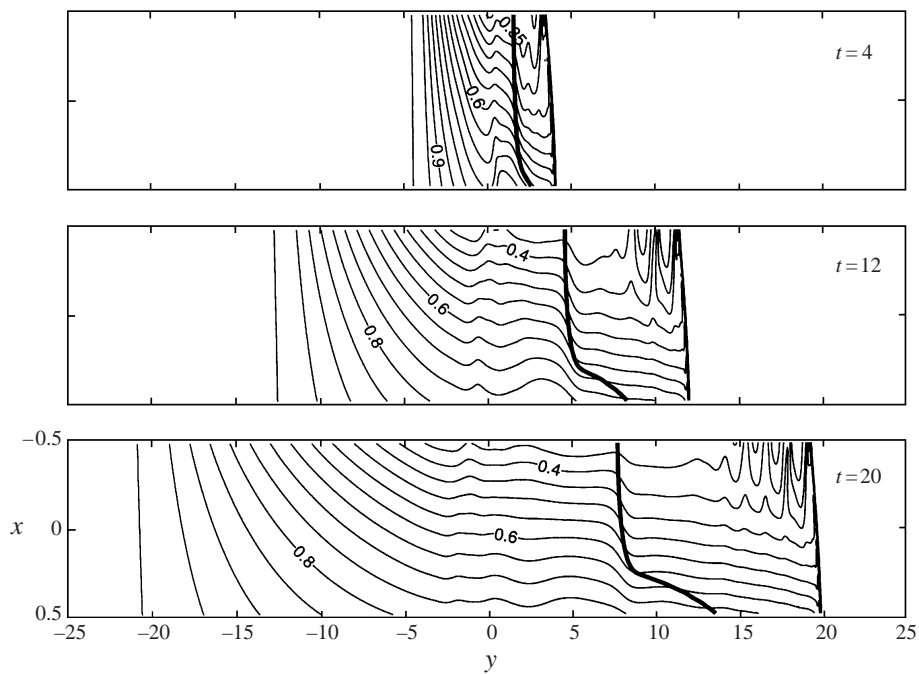FIGURE 11. Same as figure 10 except $w = 1$ and $d_0 = 0.5$.

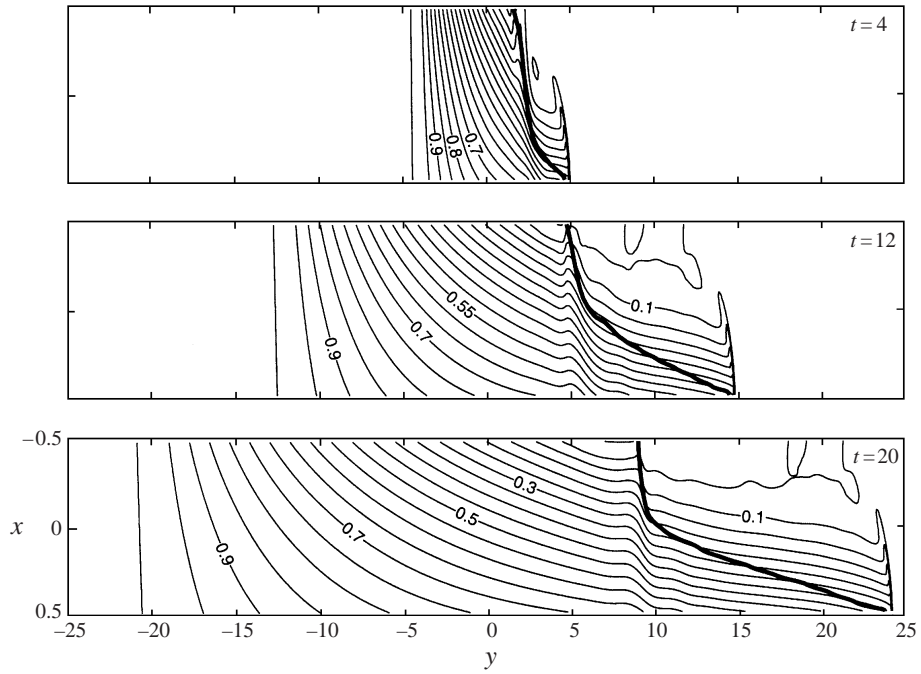FIGURE 12. Same as figure 10 except $w = 1$ and $d_0 = 0.25$.

FIGURE 13. Same as figure 10 except $w = 1$ and $d_0 = 0.05$ and a contour interval of 0.05.
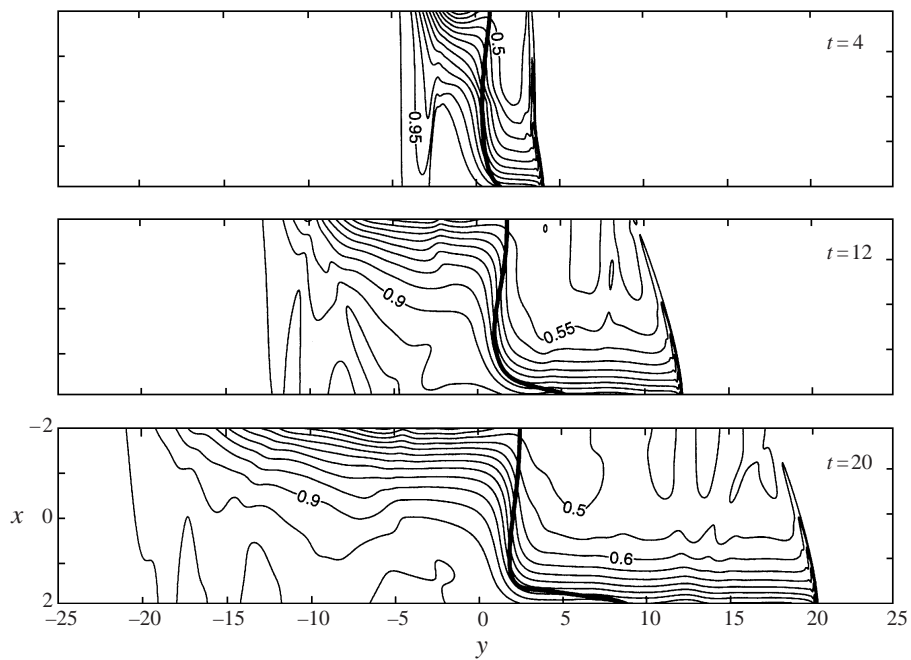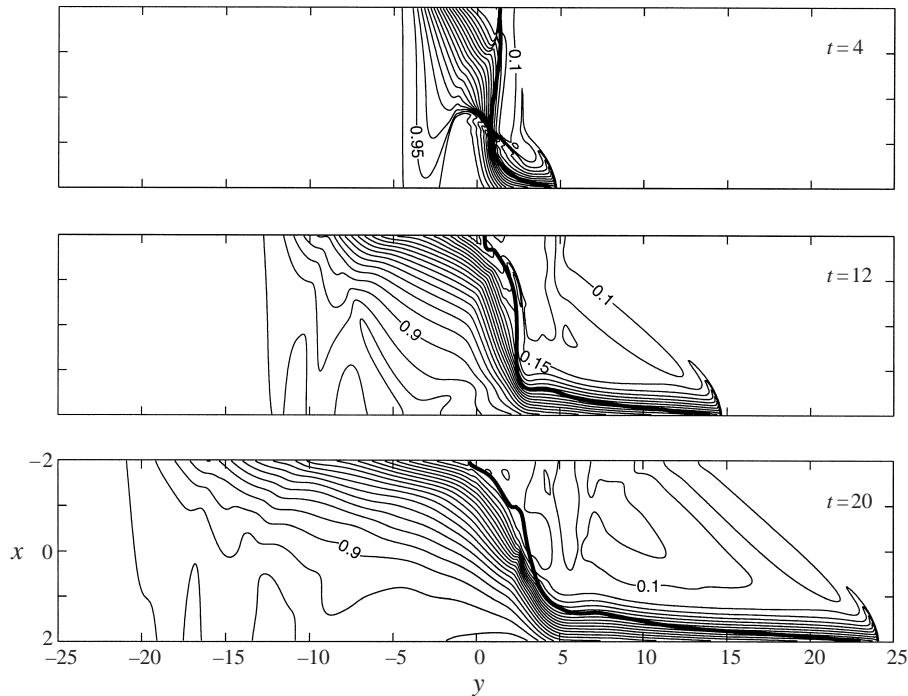

FIGURE 14. Same as figure 13 except $w = 4$ and $d_0 = 0.5$.

FIGURE 15. Same as figure 13 except $w = 4$ and $d_0 = 0.1$.

These figures illustrate most of the features found over the parameter ranges, $0 < d_0 < 1$ and $0 \leqslant w \leqslant 4$. In all cases the rarefaction wave moves upstream with speed $c_l \approx -1.05$ slightly faster the theoretical speed $c_l = -1$. This due to the lateral diffusion of momentum which tends to smooth the solution near the leading edge of the rarefaction. With smaller w and larger d_0 the shock is nearly straight across the channel. The y positions of the shock on either wall differ by less than a deformation radius. For large w or small d_0 the shock is attached to only the right-hand wall. In these cases the shock features agree qualitatively with FM's solutions for steady jumps along a coastline. For intermediate cases this distinction is more difficult to make, in part because of decaying shock amplitude away from the right-hand wall and the dissipation in the model which easily smooths small discontinuities.

An alternative categorization of the cross-channel structure of the leading jump is whether the mean depth on the left-hand wall is elevated above d_0 after the passage of the bore. Figure 16 summarizes this characteristic. In the figure we plot the channel width, normalized by the deformation radius in the shallow region, $w/\sqrt{d_0}$ versus d_0. This normalization of the width was chosen since the fluid in and immediately behind the bore has come from the still fluid ahead of the bore. If potential vorticity were conserved on passage of fluid parcels through the bore the relevant deformation radius would be based upon d_0. Even though potential vorticity is not conserved (see below) there is a clear division of behaviour based on the scaling. Cases with elevation of d on the left-hand wall are indicated by the squares. The left-hand wall is unaffected for $w/\sqrt{d_0} \gtrsim 3$ for all d_0. Those cases that cause an increase in the mean depth along the left-hand wall also correspond to bores that clearly intersect the left-hand wall within one deformation radius in y of the intersection with the right-hand wall.
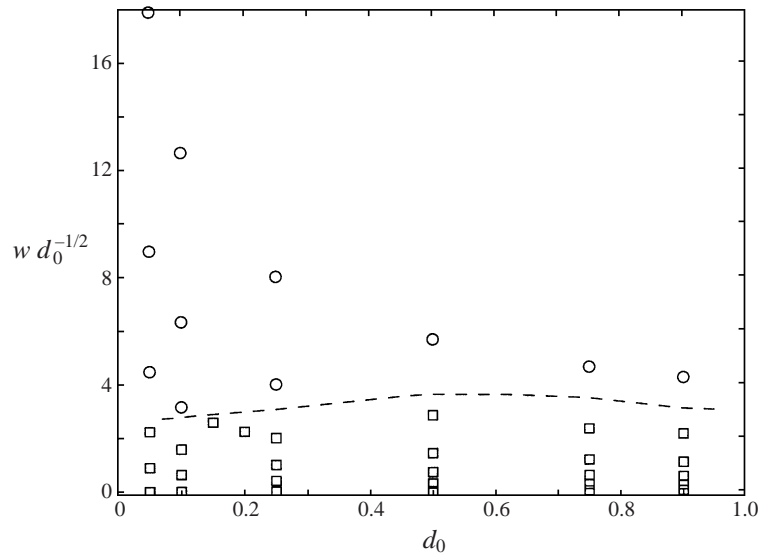
FIGURE 16. Cross-channel structure of the advancing bore as a function of $w/\sqrt{d_0}$ and d_0. The squares are for cases in which the mean depth on the left-hand wall ($x = -w/2$) immediately after passage of a bore is elevated above d_0. The circles indicate no change in mean elevation of d after passage of the bore. The dashed line indicates the approximate transition between regimes.

5.2. Shock description

The detailed structure of two bores is examined next. Figure 17 shows a close-up of d, u, v and q at $t = 20$ of the bore in figure 12 where $w = 1$ and $d_0 = 0.25$. The shock attaches normally to each wall as required by the no-normal-flow condition (Pratt 1983). The amplitude of the jump decreases away from the right-hand wall, except immediately adjacent to the left-hand wall where it increases again. The cross-channel velocity u is shown in figure 17(b). A thin boundary layer, extending the full width of the channel, of large negative u (off-shore sense if the right-hand wall is taken to be the shore) exists immediately behind the shock. Patches of alternating signs of u trailing this boundary layer are the Poincaré waves. The boundary layer connects the shock to the along-channel flow, v, behind the shock shown in figure 17(c) (Pratt 1983; FM). The layer causes a net off-shore transport of fluid. The along-channel velocity v in figure 17(c) is geostrophic except within the wave field near the left-hand wall and the layer of strong offshore flow immediately behind the jump.

Even in the inviscid limit potential vorticity q is not necessarily conserved through a bore because of the energy loss implicit in a jump (Pratt 1983). This non-conservation of q is illustrated in figure 17(d) which shows large changes of q across the jump. Near the walls q has decreased, while in the centre of the channel q has increased slightly from the value ahead of the bore $q = 1/d_0 = 4$. However, the calculation leading to figure 17(d) included explicit viscous dissipation which also causes changes in q. Schär & Smith (1993) discuss how in general changes in relative vorticity (and hence potential vorticity) are related to changes in the Bernoulli function across the jump. However, because both pseudo-inviscid and viscous process act to change the Bernoulli function across a jump it is not possible through analysis of the Bernoulli function alone to assess the relative effects of viscous processes. An estimate of the separate effects of inviscid energy loss can be made by comparison of the model results for changes in q with the relation for changes in q in inviscid systems (Pratt
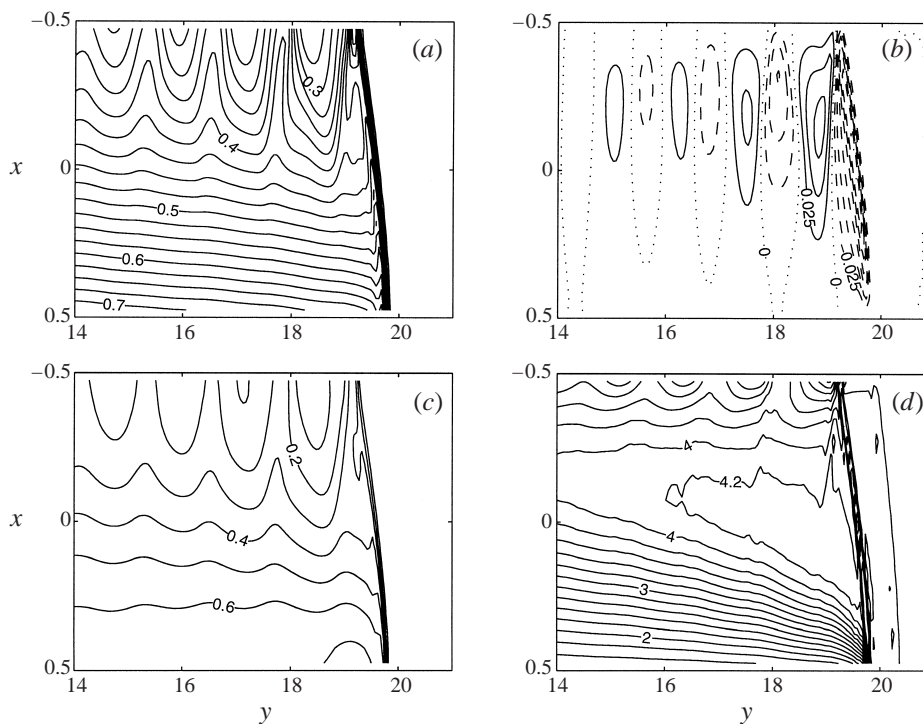
FIGURE 17. Close-up of the bore in figure 12, $w = 1$, $d_0 = 0.25$, at $t = 20$: (*a*) depth d, (*b*) cross-channel velocity u, (*c*) along-channel velocity v, (*d*) potential vorticity q. In (*b*) the solid, dashed and dotted lines indicate positive, negative and zero velocities, respectively.

1993)

$$[q] = \frac{-1}{4(u^{(n)} - c_{bore})d} \frac{\partial}{\partial s} \left(\frac{[d]^3}{d_+ d_-} \right). \tag{5.1}$$

Here $[z] = z_+ - z_-$ is the difference between z ahead of $(+)$ and behind $(-)$ the shock in the direction of the local normal. In the present notation the tangential coordinate s is aligned with the positive x-axis in the case when the shock is straight across the channel. The volume flux normal to the jump $(u^{(n)} - c_{bore})d$ in the frame moving with the steady jump speed c_{bore} is conserved across the jump.

This comparison is made in figure 18 for the bore in figure 17. The dashed line is $[q]$ evaluated from (5.1) and the solid line is $[q]$ from figure 17(*d*), with q_- at a point 0.5 units in y behind where d_- is evaluated. Changes in q along streamlines are shown. The abscissa, x_0, is the cross-channel location ahead of the bore of the streamline on which $[q]$ is evaluated. Lateral dissipation greatly affects the changes in q even to the point of causing the sign of $[q]$ from the pseudo-inviscid estimate (5.1) to be incorrect. The slip boundary conditions also contribute to $[q]$ since they permit the flux of relative vorticity through the boundary. For the conditions in figure 17 relative vorticity is fluxed out through the walls leading to a decrease in potential vorticity and an increase in $[q]$ over the pseudo-inviscid estimate. Similar differences occur in other cases. As discussed below, the lateral friction employed in the model does not greatly affect other properties of the bores.

Figure 19 shows a close-up of the shock in figure 15, $w = 4$ and $d_0 = 0.1$, at $t = 20$. In this example the jump is attached only to the right-hand wall. Note that only half
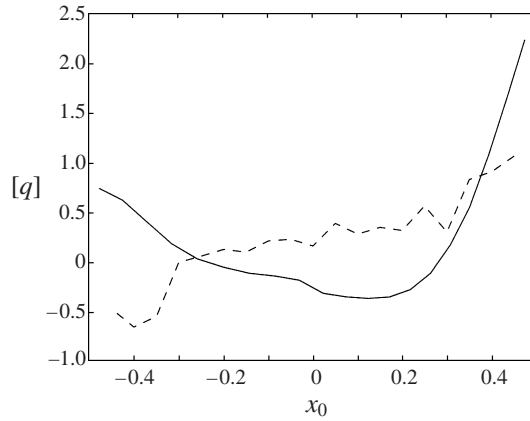
FIGURE 18. Change in potential vorticity $[q]$ across the jump in figure 17. The solid line is $[q]$ from the numerical model. The dashed line is from the 'inviscid' theory (5.1). x_0 is the cross-channel location ahead of the bore of the streamline on which $[q]$ is evaluated.
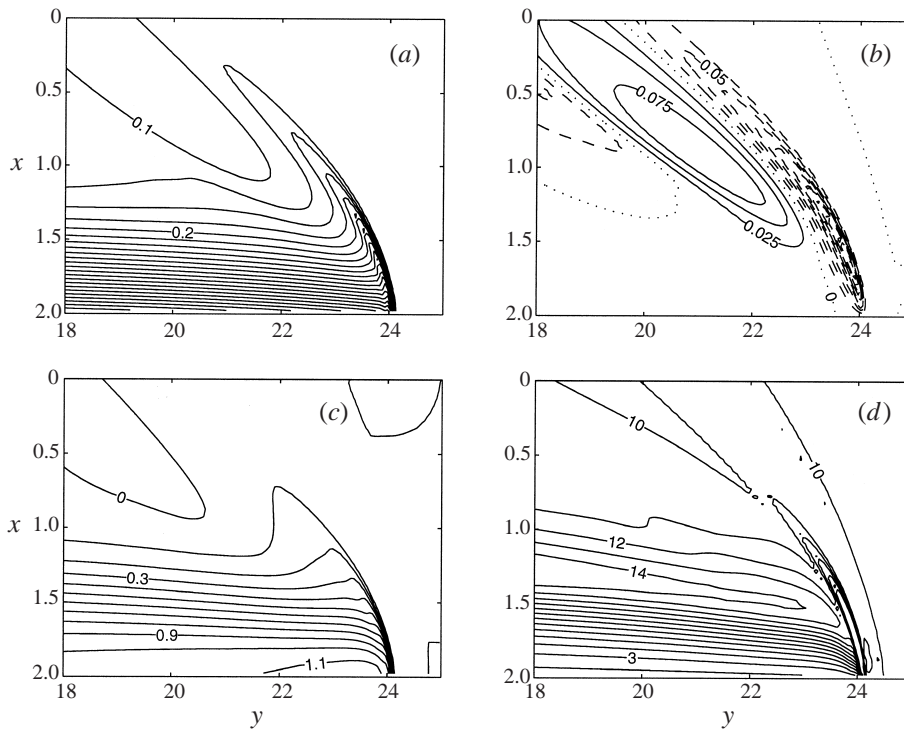

FIGURE 19. Same as figure 17 except the bore is for $w = 4$ and $d_0 = 0.1$ (figure 15 at $t = 20$).

of the channel width is shown. The general features, including the boundary layer of strong off-shore flow and potential vorticity structure, are similar to the example in figure 17.

Since rotation causes the maximum shock height to be on the right-hand wall we take the difference in depths immediately upstream and downstream of the discontinuity on the right-hand wall to define the bore amplitude $\delta d_{bore} = [d]$. This definition does not include the smoother increase in d across the boundary layer
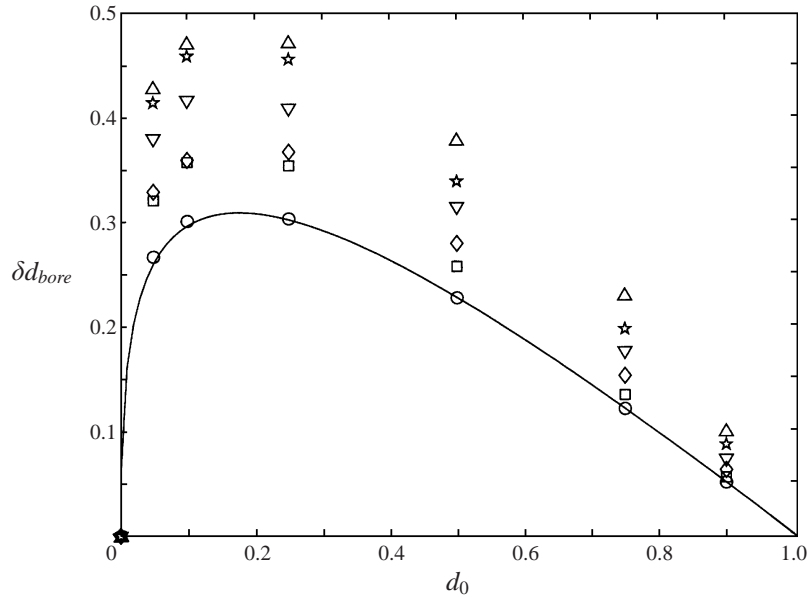
FIGURE 20. The bore amplitude δd_{bore} as a function of d_0: $w = 0$ ($\bigcirc$), 0.2 ($\square$), 0.5 ($\diamond$), 1 ($\triangledown$), 2 ($\star$), 4 ($\triangle$). The non-rotating ($w = 0$) theory is the solid line.

behind the bore and is the same definition of jump amplitude used by FM. FM's steady, weakly nonlinear theory for bore structure gave a depth increase across the boundary layer of $\frac{1}{3}\delta d_{bore}$. We do not find any constant relation between the depth increase across the trailing boundary layer and δd_{bore}. This is likely to be due to finite-amplitude effects and unsteadiness of the flow behind the bore.

Because of the lateral friction and possibly due to the radiation of Poincaré waves the amplitude of the shock decreased slowly with distance. Decay did not occur for the non-rotating runs and only became apparent for $w \geqslant 1$ and d_0 small (3–5% decrease in δd_{bore} from $t = 5$ to 20). We use δd_{bore} at $t = 10$ to define the bore amplitude. This is after the bore has reached a quasi-steady state and before any significant dissipation occurs. Figure 20 shows how δd_{bore} depends on d_0. Stoker's non-rotating solution is plotted as the solid line. The numerical results for no rotation agree quite well with the theory. Rotation causes the amplitude to increase with w. The shape of the relation between δd_{bore} and d_0 for a given w is similar to the non-rotating solution. The maximum in δd_{bore} also occurs near the point of maximum amplitude when there is no rotation.

The bore speed c_{bore} along the right-hand wall (at $t = 10$) is plotted in figure 21. The speeds for small d_0 with no rotation are slightly less than non-rotating theory predicts. This is due almost entirely to the lateral dissipation in the model. Reducing dissipation results in better agreement at the expense of oscillations (dispersive numerical errors) immediately behind the shock. Rotation causes c_{bore} to increase above the non-rotating speed, though for $w < 1$ the effect is very weak. Again the qualitative dependence on d_0 is similar to the non-rotating theory, though for $w = 4$ there is no minimum in c_{bore} as d_0 decreases.

In a non-rotating system the speed of a shock advancing into resting fluid of depth d_0 is, in dimensional variables, (Stoker 1957)
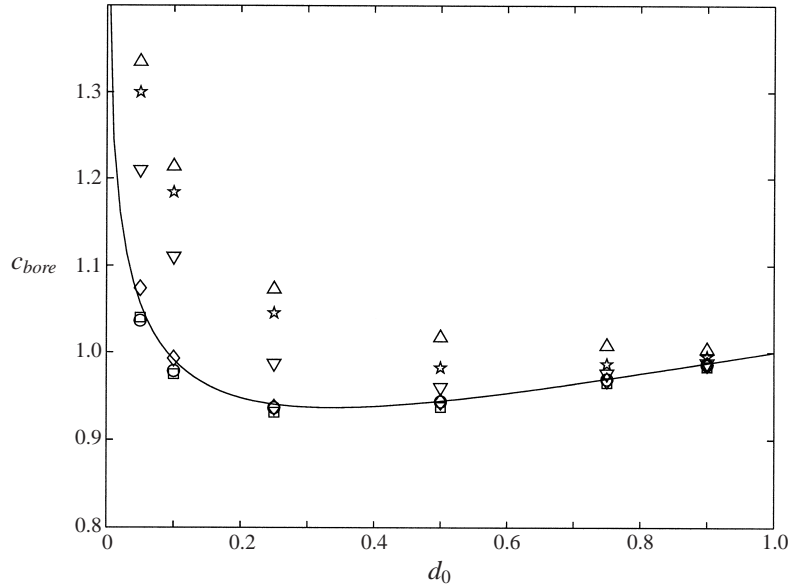
$$c_{bore}^2 = gd_0(1 + A)(1 + \tfrac{1}{2}A), \tag{5.2}$$

FIGURE 21. The bore speed c_{bore} as a function of d_0: $w = 0$ ($\bigcirc$), 0.2 ($\square$), 0.5 ($\diamond$), 1 ($\triangledown$), 2 ($\bigstar$), 4 ($\triangle$). The non-rotating ($w = 0$) theory is the solid line.

where $A = \delta d_{bore}/d_0$. This relation (with A evaluated on the right-hand wall) was also obtained by FM for finite-amplitude jumps with rotation in an infinitely wide channel. In figure 22 we show c_{bore}, normalized by the non-dimensional speed of linear waves in the resting fluid ahead of the shock $\sqrt{d_0}$, as a function of A. The non-rotating runs agree quite well with (5.2). However, adding rotation results in lower speeds than predicted from (5.2). For $A < 1$ (inset) the speeds do approach (5.2) as w decreases. But for $A > 1$ this dependence on w is not obvious for the widths examined. The speeds appear to branch from the non-rotating speed as the channel width is increased, and the departure is more rapid the larger the bore amplitude.

Some of the difference between the numerical results and (5.2) might be attributed to numerical errors in the model or lateral dissipation. To test this several runs with a more accurate numerical model with no explicit lateral dissipation were made using the fourth-order in space, third-order in time ENO scheme described in Rogerson (1999). That model, which could not be used in cases that developed layer depths near zero, gave shock speeds and amplitudes that were slightly larger (3–5% in the worst cases) than the results from our numerical model. However, the speed versus amplitude points also fell below (5.2) and were along the trends in figure 22. Other features of the flow, such as Poincaré wave generation behind the shock, were found with both numerical methods.

It is worth noting that FM obtain (5.2) from an equation ((7.21) in FM) for the cross-channel gradient of the along-channel shock position. In our notation this equation is

$$\left(\frac{dR}{dx}\right)^2 = \frac{c_{bore}^2}{gd_0(1 + A)(1 + \frac{1}{2}A)} - 1,$$

where $R(x)$ is the along-channel position of the shock and $A = A(x)$ is the local jump amplitude. Requiring the shock to attach normally to the right-hand wall,
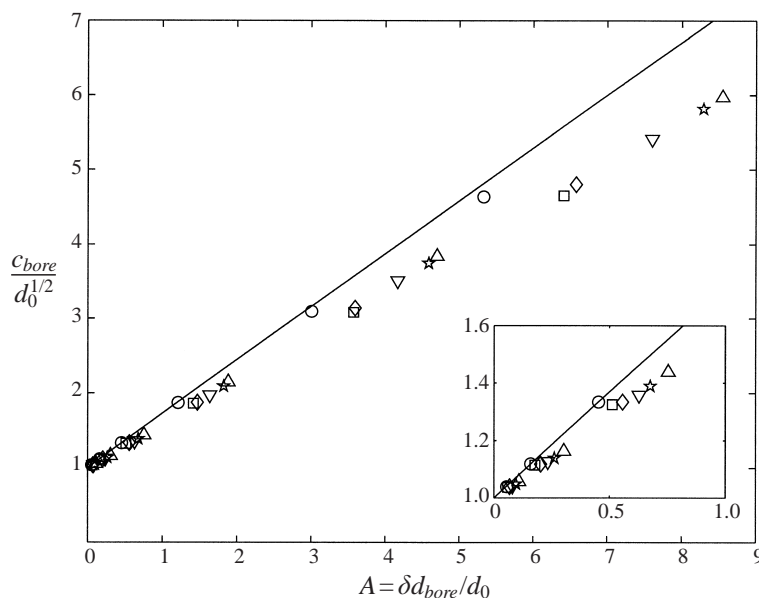
FIGURE 22. $c_{bore}/\sqrt{d_0}$ as a function of bore amplitude $A = \delta d_{bore}/d_0$. The solid line is from (5.2) and the symbols are the numerical results for $w = 0$ ($\bigcirc$), 0.2 ($\square$), 0.5 ($\diamond$), 1 ($\triangledown$), 2 ($\bigstar$), 4 ($\triangle$). The inset shows a close-up for $A < 1$.

$R_x|_{x=w/2} = 0$, leads to (5.2). In a finite-width channel the requirement of normal contact on the left-hand wall also gives (5.2), with A now evaluated on the left-hand wall. Steady bores which contact both walls must give the same value for c_{bore} and can only occur if the jump amplitudes on the left- and right-hand walls are equal. Our calculations do not give equal wall amplitudes, implying that there may be no steady solutions. This is consistent with radiation of Poincaré waves which continually drain energy from the bores.

In addition to the Poincaré wave radiation observed for some of the numerical bores, there are several other possible explanations for the discrepancy with the speeds predicted by (5.2). Even the bores which exhibited no noticeable radiation did not propagate in a completely steady manner, though variations in speed amounted to no more that a few tenths of a percent per rotation period. Also, the numerical bores in the wider channels were observed to be more dispersive than the fully nonlinear coastal solutions of FM. Their steady, inviscid solutions exhibit a depth discontinuity arbitrarily far from the coast whereas this discontinuity disappears a finite distance from the right-hand wall in our numerical solutions. This is attributable to both the unsteadiness and dissipation in the present calculations.

Other aspects of FM's theory agree qualitatively with our numerical results. In wide channels the angle the shock makes with the x-axis far from the wall increases with bore amplitude as illustrated in figures 14 and 15. The cross-channel decay of the shock and trailing geostrophic flow increases with shock speed and scales with the local deformation radius c_{bore}/f, with c_{bore} from (5.2).

5.3. *Advection of new fluid down the channel*

The speeds of the intersection of the new fluid interface ($c = 0.5$ contour) along the right- and left-hand walls evaluated at $t = 20$ are shown in figure 23. Figure 23(a) shows that increasing w while holding d_0 fixed, or decreasing d_0 while holding w fixed,
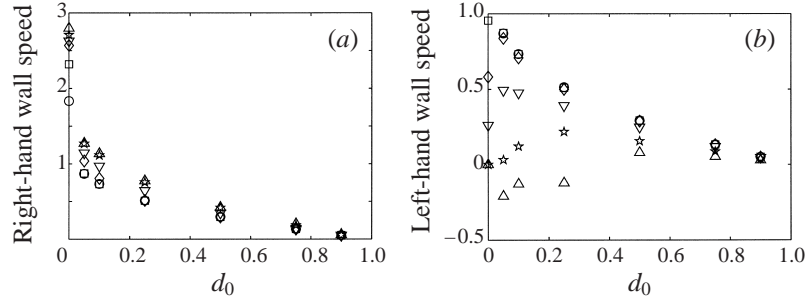
FIGURE 23. Speed of the $c = 0.5$ contour on the right (a) and the left-hand wall (b) as a function of d_0. $w = 0$ ($\bigcirc$), 0.2 ($\square$), 0.5 ($\Diamond$), 1 ($\bigtriangledown$), 2 ($\bigstar$), 4 ($\triangle$).

results in faster propagation of new fluid along the right-hand wall. The speeds along the left-hand wall are shown in figure 23(b). Not surprisingly, the interface always advances fastest along the right-hand wall. For $d_0 > 0.5$ the fluid always advances downstream along both channel walls and our results agree qualitatively with HRJ.

We see only minor indications of the interface advancing faster along the left-hand wall than in the middle of the channel (cf. figure 14). This was a common feature of both HRJ's quasi-geostrophic contour dynamics and shallow water equation solutions. HRJ also found cases where the interface along the right-hand wall would pinch off to form a detached parcel of fluid. We found no evidence of this behaviour. However, these numerical experiments did not advance very far in the small time scaling used by HRJ and these features may not have had time to develop. Also significant is the difference in lateral boundary conditions between these studies. We employ slip conditions which permit the flux of relative vorticity through the walls, while HRJ's shallow water simulations used superslip conditions that allow the flux of momentum, but not vorticity, through the walls. The superslip conditions are in keeping with their contour dynamics model which conserves potential vorticity.

One new feature resulting from the finite-amplitude initial conditions is that for $w \geqslant 2$ the speed of advancement along the left-hand wall decreases as d_0 is decreased below about 0.5, and can even become negative. Also, preferential intrusion of new fluid along the right-hand wall can be achieved not only by increasing w, but also by reducing d_0 for fixed w, even for relatively narrow channels. This is not surprising since for $d_0 \to 0$ all fluid advancing down the channel was originally behind the dam.

5.4. *Mean transport*

Before discussing the mean downstream transport Q at $y = 0$ it is interesting to consider the transient behaviour. When $w > 0.5$ the transport undergoes weakly decaying oscillations. The period, amplitude and decay time scale of the oscillations increase with increasing w or decreasing d_0. These characteristics agree qualitatively with the linear solution (Gill 1976). The frequency σ of the oscillations, when they occur, is given to within $\pm 20\%$ by the frequency of the linear Poincaré waves (Pedlosky 1987) with lowest cross-channel mode, zero along-channel wavenumber and depth equal to the average of the initial levels on either side of the dam $(1 + d_0)/2$,

$$\sigma^2 = 1 + \frac{1 + d_0}{2} \left(\frac{\pi}{w} \right)^2.$$

The agreement with the linear estimate is surprising since the basic state on which the waves exists has large lateral variations in velocity and depth.
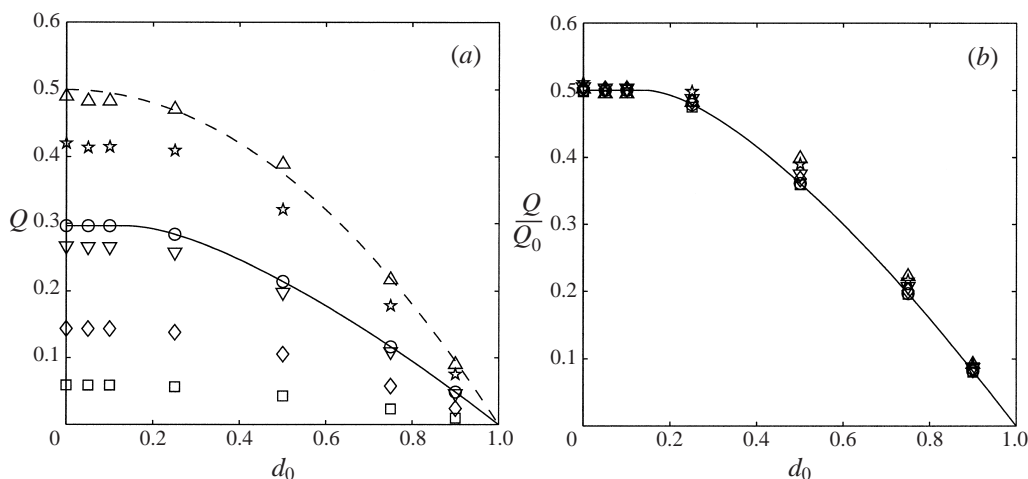
FIGURE 24. The mean transport Q as a function of d_0 and w. In (*a*) the solid line is the non-rotating theory for a channel of unit width and the dashed line is the geostrophic transport $Q = (1 - d_0^2)/2$. In (*b*) the transport is normalized by the transport from the semigeostrophic theory for $d_0 = 0$, Q_0. The solid line is again the non-rotating result. In both (*a*) and (*b*) $w = 0$ (○), 0.2 (□), 0.5 (◇), 1 (▽), 2 (★), 4 (△).

The mean transport (averaged over several oscillation periods) is shown in figure 24. Figure 24(*a*) shows how Q depends on d_0 and w. For fixed w the maximum transport occurs for $d_0 = 0$. The solid curve is the non-rotating result for a channel of unit width and the circles are the corresponding model result. The dashed curve is the 'geostrophic control' bound , $Q = (1 - d_0^2)/2$ predicted by Toulany & Garrett (1984). Note that this bound is slightly exceeded for $w = 4$ at intermediate values of d_0. The Q versus d_0 dependence for any w is similar to the non-rotating theory and the increase in Q with w for a fixed d_0 is similar to the semigeostrophic theory for $d_0 = 0$. This suggests figure 24(*b*) where $Q(w, d_0)$ is scaled by $Q_0(w) = Q(w, 0)$, the transport for zero upstream depth. The transports now nearly collapse to the scaled non-rotating curve.

6. Discussion

We have studied the strongly nonlinear and time-dependent regimes of Rossby adjustment in a channel created when the initial depth difference is large. Using the semigeostrophic approximation and the method of characteristics semi-analytical solutions have been obtained in the extreme case when the fluid depth downstream of the barrier is zero. These solutions were explored and compared to numerical calculations of the full shallow water equations with generally good agreement. The numerical solutions highlight the failure of the semigeostrophic approximation in the limit of wide channels. The failure is related to the occurrence of large cross-channel velocities and oscillations. Even though the semigeostrophic theory failed to reproduce some of the complicated time-dependent features for wide channels, the steady-state flows agree with the numerically computed solutions. This is a reassuring result since much of our understanding of steady hydraulically controlled flows under the influence of rotation (e.g. Gill 1977) has been obtained with the powerful simplification of the semigeostrophic approximation. It does imply, though, that studies of time-dependent processes may require the full shallow water equations.

For zero initial downstream depth the fluid intrudes down the channel preferentially along the right-hand wall at a speed which increases with channel width from the theoretical non-rotating speed of $2\sqrt{gD}$ to a maximum of $3.80\sqrt{gD}$. However, laboratory experiments of the comparable dam break problem in two-layer systems by Stern *et al.* (1982), Kubokawa & Hanawa (1984*b*) and Griffiths & Hopfinger (1983) give speeds well below these. Stern *et al.* and Kubokawa & Hanawa find $c_{nose} \approx \sqrt{g'D}$ and Griffiths & Hopfinger find $c_{nose} \approx 1.3\sqrt{g'D}$, where g' is the reduced gravity. Not only are the speeds different, the nose is bulbous and turbulent. The differences are certainly associated with the presence of the second layer. This is not surprising since even in the non-rotating case the theoretical single-layer nose speed is well above laboratory observations which show $c_{nose} \approx \sqrt{g'D}$ (Simpson 1987). Klemp, Rotunno & Skamarock (1993) discuss the use of Benjamin's (1968) flow force analysis for gravity currents to correct the nose speed in the non-rotating dam break problem. In the rotating experiments some of the same considerations apply as Stern *et al.* (1982) and Griffiths & Hopfinger (1983) point out. Other complications arise in the rotating problem. These include lateral mixing, baroclinic instability and radiation of inertial waves in the second layer, all of which have been argued to be important in the dynamics of rotating gravity currents (Griffiths 1986). Thus the semigeostrophic solutions for the nose speed may have limited application in two-layered systems. However, other aspects of the solutions well behind the nose are unaffected by the details of the nose dynamics since the flow is supercritical. We consider the single-layer zero-downstream-depth case to be a basis for further studies of time-dependent rotating hydraulic flows. For example, it should be possible to include the Benjamin-type analysis for the rotating gravity current developed by Stern *et al.* (1982) in the semigeostrophic method of characteristic solution as Klemp *et al.* (1994) did for the non-rotating problem.

When the downstream depth is finite the rarefying nose is replaced by a shock or bore. The evolving flow behind the bore departs from the linear and weakly nonlinear cases. The dynamics of the numerically computed shock solutions were compared to existing theories of rotating shocks and jumps. Qualitative agreement was found including the presence of a boundary layer of strong off-shore flow immediately behind the shock. Still, significant open questions remain. The observed shock speed dependence on amplitude was not as predicted by FM's finite-amplitude theory for infinitely wide channels. We have not been able to resolve this issue but suspect that the answer resides in both the finite width of the channel and that the integration of the momentum and continuity equations across the jump must be done over a region large enough to include the rotationally influenced boundary layer immediately behind the shock. This is difficult since non-local Coriolis terms must be retained in the resulting integral conditions. When the upstream flow is not at rest these boundary layers may exist on both sides of the jump (Pratt 1983). Nof (1986) finds some jump solutions in narrow channels ($w \ll 1$) which do not require boundary layers. However, these solutions occur only for special combinations of upstream and downstream geostrophic flows.

Our numerical results confirmed that potential vorticity is not conserved across the jump. Further, the changes are sensitive to the explicit dissipation in the model. This is consistent with Schär & Smith (1993) who discussed potential vorticity production in non-rotating dissipative hydraulic flows. The interesting result from our modelling is that the sign of the change in potential vorticity can be opposite to the 'inviscid' estimate due to the effects of the explicit dissipative vorticity flux. This poses a significant problem for efforts to model potential vorticity variations in deep

hydraulically controlled overflows, for example, since the strength and mechanism of the dissipation is unknown. We have considered just one form of lateral mixing as a crude approximation to reality and have not considered vertical mixing and bottom friction which are known to be important in overflows (Baringer & Price 1997).

Previous tests (Whitehead 1986; Wright 1987) of the transport bound suggested by the principle of geostrophic control (Toulany & Garrett 1984) have largely been based on linear or nearly linear systems in which the elevation difference between reservoirs is relatively small. Our study, which has no such restriction, confirms the transport bound, $(g/2f)(d_u^2 - d_d^2)$, but only when d_u and d_d are chosen as the initial depths or when the channel is infinitely wide. In practical applications such as sea straits, the initial conditions are unknown, the throughflow is often statistically steady, and one or both of the bounding basins have finite extent. As suggested by Pratt (1991) the above transport bound may still be valid when applied over finite time scales. For example the values of d_u and d_d might independently fluctuate due, say, to tides or atmospheric forcing. An incremental change in elevation difference $d_u - d_d$ causes the flow to adjust in a manner qualitatively similar to what occurs in the dam break problem. A new transport is established after a time delay of $O(f^{-1})$, the time required for Kelvin waves to form and separate in the strait. If the separation point (marking the location where the boundary layer crosses the strait) remains in the strait and is not swept into the downstream basin, then the transport produced by this delay should be bounded by the value based on the current d_u and d_d. Our calculations have shown that the downstream movement of the separation point for channel widths more than a few deformation radii wide is very slow, suggesting that the bound is valid for similarly wide basins. Of course, if the observer then waits long enough and if there are no further forced changes in d_u and d_d, the separation point will drift downstream, the value of $d_u - d_d$ will relax to zero, and the bound will become invalid. Or one of the Kelvin waves produced by the initial adjustment may propagate around the edge of one of the basins and return to the strait. In summary, the geostrophic control bound may be practical over time scales long compared to f^{-1} but short compared to both the intrinsic advective time of the separation point and the travel time of a Kelvin wave around the smallest basin.

Appendix. Numerical method

Numerical methods for treating the rapid flow transitions common in hydraulics problems must allow shocks to form in a numerically stable manner and must enforce conservation of certain integral quantities (usually volume and momentum flux) across the shocks. In two-dimensional rotating hydraulics, flow separation from one wall or the topography (i.e. zero layer depth) is common and must also be accommodated. There are very accurate methods for shock capturing that take advantage of the hyperbolic nature of the single-layer shallow water equations (2.1)–(2.3). These include Godunov's method (Leveque 1997) and essentially non-oscillatory (ENO) techniques (Shu & Osher 1988). However, when the layer depth becomes zero, particularly over

topography, these methods tend to fail. The problem is no longer totally hyperbolic when the characteristic speeds coalesce at zero depth.

Since shocks and separated flows are integral to this study we have employed a finite-volume numerical method using the cell-centred flux-corrected transport (FCT) method that follows closely the method Schär & Smith (1993) used in their study of shallow, non-rotating flow past topography. The model solves the non-dimensional single-layer shallow water equations in flux form,

$$\frac{\partial}{\partial t}(ud) + \frac{\partial}{\partial x}\left(u^2 d + \tfrac{1}{2}d^2\right) + \frac{\partial}{\partial y}(uvd) - vd = 0, \tag{A 1}$$

$$\frac{\partial}{\partial t}(vd) + \frac{\partial}{\partial x}(uvd) + \frac{\partial}{\partial y}\left(v^2 d + \tfrac{1}{2}d^2\right) + ud = 0, \tag{A 2}$$

$$\frac{\partial d}{\partial t} + \frac{\partial}{\partial x}(ud) + \frac{\partial}{\partial y}(vd) = 0, \tag{A 3}$$

and so obeys discrete forms of mass and momentum flux across discontinuities. The non-dimensionalization is the same as in (2.1)–(2.3) with $\delta^2 = 1$. Layer depths approaching zero (limited to a minimum depth of 10^{-10} to avoid division by zero) are allowed. The main difference between our method and the scheme used by Schär & Smith (1993) is the replacement of the MPDATA algorithm (Smolarkiewicz & Clark 1986) for computing the advective fluxes with the simpler and more efficient slope-limited FCT method for advection equations in flux form described in Leveque (1997). The formulation is second-order accurate in space and time. We also employ an upwind treatment of the advective form of the momentum equations for the estimation of the cell-face velocities at the half time-step.

The lateral dissipation terms

$$F_u = v\nabla \cdot (d\nabla u), \quad F_v = v\nabla \cdot (d\nabla v)$$

are included on the right-hand sides of (A1) and (A2), respectively. Here v is a constant friction coefficient. This form of the dissipation was chosen to guarantee that internal dissipation does not create or destroy momentum and is treated numerically to avoid dissipative momentum flux to grid cells with nearly zero depth (Schär & Smith 1993). Friction is included primarily to help control oscillatory behaviour in the immediate vicinity of a discontinuity. All the results in this paper used $v = 0.005$, a value large enough to eliminate much of the oscillatory behaviour, but not large enough to significantly affect shock behaviour.

No-flux conditions were imposed on the channel sidewalls ($x = \pm w/2$) and Orlanski (1976) radiation conditions were used at the ends of the channel. The channel walls were treated as slip boundaries ($\partial v/\partial x = 0$) to keep the calculations close to the inviscid theories.

The model was tested by comparisons with analytical solutions for shock propagation formation in non-rotating one-dimensional flow. These tests included the non-rotating dam break problem and the results are discussed in §4 and §5. While spurious oscillations at discontinuities are not completely eliminated, they do not grow and result in numerical instabilities. The behaviour of a contact line between wet and dry regions was tested by examining the spreading of a drop of water under gravity (Schär & Smolarkiewicz 1996) and with the solutions of Carrier & Greenspan (1958) for run-up of non-rotating nonlinear shallow water waves on a slope, with very good results in both cases.

For the numerical experiments described in this paper, a uniform cell-centred grid

was used with grid spacing in y of $\Delta y = 0.05$. The spacing in the cross-channel direction, Δx, was a maximum of 0.05, and for the runs with zero upstream depth or narrow channels it was typically less. The time step Δt was typically 0.01.

REFERENCES

BARINGER, M. O. & PRICE, J. 1997 Momentum and energy balance of the Mediterranean outflow. *J. Phys. Oceanogr.* **27**, 1678–1692.

BENJAMIN, T. B. 1968 Gravity currents and related phenomena. *J. Fluid Mech.* **31**, 209–248.

CARRIER, G. F. & GREENSPAN, H. P. 1958 Water waves of finite amplitude on a sloping beach. *J. Fluid Mech.* **4**, 97–109.

CEDERLF, U. E. B., LUNDBERG, P. A. & STERHUS, S. 1989 Hydrographical evidence for an isopycnal intrusion corroborated by acoustic doppler current profiling. *J. Geophys. Res.* **98**(C8), 10839–10843.

FEDOROV, A. V. & MELVILLE, W. K. 1996 Hydraulic jumps at boundaries in rotating fluids. *J. Fluid Mech.* **324**, 55–82 (referred to herein as FM).

GILL, A. E. 1976 Adjustment under gravity in a rotating channel. *J. Fluid Mech.* **77**, 603–621.

GILL, A. E. 1977 The hydraulics of rotating-channel flow. *J. Fluid Mech.* **80**, 641–671.

GILL, A. E. 1982 *Atmospheric-Ocean Dynamics.* Academic.

GRIFFITHS, R. W. 1986 Gravity currents in rotating systems. *Ann. Rev. Fluid Mech.* **18**, 59–89.

GRIFFITHS, R. W. & HOPFINGER, E. J. 1983 Gravity currents moving along a lateral barrier in a rotating fluid. *J. Fluid Mech.* **134**, 357–399.

HERMANN, A. J., RHINES, P. & JOHNSON, E. R. 1989 Nonlinear Rossby adjustment in a channel: beyond Kelvin waves. *J. Fluid Mech.* **205**, 469–502 (referred to herein as HRJ).

KLEMP, J. B., ROTUNNO, R. & SKAMAROCK, W. K. 1994 On the dynamics of gravity currents in a channel. *J. Fluid Mech.* **269**, 169–198.

KUBOKAWA, A. & HANAWA, K. 1984a A theory of semigeostrophic gravity waves and its application to the intrusion of a density current along a coast. Part 1. Semigeostrophic gravity waves. *J. Oceanogr. Soc. Japan* **40**, 247–259.

KUBOKAWA, A. & HANAWA, K. 1984b A theory of semigeostrophic gravity waves and its application to the intrusion of a density current along a coast. Part 2. Intrusion of a density current along a coast of a rotating fluid. *J. Oceanogr. Soc. Japan* **40**, 260–270.

LEVEQUE, R. J. 1997 Wave propagation algorithms for multidimensional hyperbolic systems. *J. Comput. Phys.* **131**, 327–353.

LONG, R. R. 1954 Some aspects of the flow of stratified fluids. II. Experiments with a two-fluid system *Tellus* **6**, 97–115.

LONG, R. R. 1955 Some aspects of the flow of stratified fluids. III. Continuous Density Gradients. *Tellus* **7**, 341–357.

LONG, R. R. 1970 Blocking effects in flow over obstacles. *Tellus* **22**, 471–480.

MELVILLE, W. K., TOMASSON, G. G. & RENOUARD, D. P. 1989 On the stability of Kelvin waves. *J. Fluid Mech.* **206**, 1–23.

NOF, D. 1986 Geostrophic shock waves. *J. Phys. Oceano.* **16**, 886–901.

ORLANSKI, I. 1976 A simple boundary condition for unbounded hyperbolic flows. *J. Comput. Phys.* **21**, 251–269.

PEDLOSKY, J. 1987 *Geophysical Fluid Dynamics.* Springer.

PRATT, L. J. 1983 On inertial flow over topography. Part 1. Semigeostrophic adjustment to an obstacle. *J. Fluid Mech.* **131**, 195–218.

PRATT, L. J. 1991 Geostrophic versus critical control in straits. *J. Phys. Oceanogr.* **21**, 728–732.

ROGERSON, A. 1999 Transcritical flows in the coastal marine atmospheric layer. *J. Atmos. Sci.* (in press).

ROSSBY, C. G. 1937 On the mutual adjustment of pressure and velocity distributions in certain simple current systems I. *J. Mar. Res.* **1**, 15–28.

SCHÄR, C. & SMITH, R. B. 1993 Shallow-water flow past isolated topography. Part I: Vorticity production and wake formation. *J. Atmos. Sci.* **50**, 1373–1400.

SCHÄR, C. & SMOLARKIEWICZ, P. K. 1996 A synchronous and iterative flux-correction formalism for coupled transport equations. *J. Comput. Phys.* **128**, 101–120.

SHU, C. W. & OSHER, S. 1988 Efficient implementation of essentially non-oscillatory shock capturing schemes. *J. Comput. Phys.* **77**, 439–471.

SIMPSON, J. E. 1987 *Gravity Currents: In the Environment and the Laboratory*. Ellis Horwood.

SMITH, P. C. 1976 Baroclinic instability in the Denmark Strait. *J. Phys. Oceanogr.* **6**, 355–371.

SMOLARKIEWICZ, P. K. & CLARK, T. L. 1986 The multidimensional positive definite advection transport algorithm: Further development and applications. *J. Comput. Phys.* **67**, 396–438.

STERN, M. E., WHITEHEAD, J. A. & HUA, B. L. 1982 The intrusion of a density current along the coast of a rotating fluid. *J. Fluid Mech.* **123**, 237–265.

STOKER, J. J. 1957 *Water Waves*. Interscience.

TOMASSON, G. G. & MELVILLE, W. K. 1992 Geostrophic adjustment in a channel: nonlinear and dispersive effects. *J. Fluid Mech.* **241**, 23–58.

TOULANY, B. & GARRETT, C. J. R. 1984 Geostrophic control of fluctuating flow through straits. *J. Phys. Oceanogr.* **14**, 649–655.

WATTS, R. G. & HAYDER, M. E. 1983 Climatic fluctuations due to deep-ocean circulation. *Science* **219**, 387–388.

WHITEHEAD, J. A. 1986 Flow of a homogeneous rotating fluid through straits. *J. Geophys. Astrophys. Fluid Dyn.* **36**, 187–205.

WHITEHEAD, J. A., LEETMA, A. & KNOX, R. A. 1974 Rotating hydraulics of strait and sill flows. *Geophys. Fluid Dyn.* **6**, 101–125.

WHITHAM, G. B. 1974 *Linear and Nonlinear Waves*. John Wiley.

WRIGHT, D. G. 1987 Comments on 'Geostrophic control of fluctuating barotropic flow through straits'. *J. Phys. Oceanogr.* **17**, 2375–2377.